

VYSOKÉ UČENÍ TECHNICKÉ V BRNĚ
BRNO UNIVERSITY OF TECHNOLOGY



FAKULTA STROJNÍHO INŽENÝRSTVÍ
ÚSTAV FYZIKÁLNÍHO INŽENÝRSTVÍ
FACULTY OF MECHANICAL ENGINEERING
INSTITUTE OF PHYSICAL ENGINEERING

OPTIMALIZACE PROCEDURY MĚŘENÍ OPTICKÉHO ZÁŘENÍ ROZPTÝLENÉHO PEVNÝMI TĚLESY PROVÁDĚNÉHO SCATTERMETEREM

OPTIMIZING MEASUREMENT PROCEDURE OF THE OPTICAL RADIATION SCATTERED BY
SOLID SURFACE PERFORMED BY THE SCATTERMETER

DIPLOMOVÁ PRÁCE
MASTER'S THESIS

AUTOR PRÁCE
AUTHOR

Bc. JAKUB KLUS

VEDOUCÍ PRÁCE
SUPERVISOR

prof. RNDr. MILOSLAV OHLÍDAL, CSc.

Abstrakt

Tato práce se zabývá optimalizací procedury měření optického záření rozptýleného pevnými tělesy prováděného pomocí scatterometru. V práci je popsáno několik metod použitelných k nalezení souboru pozic nepřekrývajících se kruhových detektorů na povrchu polokoule (i koule). Výsledky práce jsou aplikovány na samotný měřicí přístroj a je ukázána shoda experimentálních výsledků získaných před i po optimalizaci. Výhodu nového uspořádání lze nalézt především v převedení dřívějšího způsobu měření na soubor nezávislých měření, což má význam pro matematické zpracování výsledků.

Summary

This work concerns with optimizing the measurement procedure of the optical radiation scattered from a solid surface performed by the scattermeter. The major part is devoted to the description of methods of finding set of positions of non-overlapping circular detectors on a surface of a hemisphere (or a sphere). Results of the optimization are applied to the measurement device. The agreement of the previous and new measurement procedures is shown in the end of this work. The crucial advantage of the new procedure is that the new set of point allows us to treat the measured values independently. This is useful for the mathematical processing of the results.

Klíčová slova

Rozptyl elektromagnetického záření, scattermeter, drsné povrchy, solární články

Keywords

Scattering of the electromagnetic radiation, scattermeter, rough surfaces, solar cells

KLUS, J. *Optimalizace procedury měření optického záření rozptýleného pevnými tělesy prováděného scattermeterem*. Brno: Vysoké učení technické v Brně, Fakulta strojního inženýrství, 2013. 60 s. Vedoucí prof. RNDr. Miloslav Ohlídál, CSc.

Hereby I declare that I have created this work autonomously under a scientific supervision of Prof. Miloslav Ohlídál. All sources, references and literature used or excerpted during the elaboration of this work are properly cited and listed in the complete reference.

Bc. Jakub Klus

I would like to thank to my supervisor Prof. Miloslav Ohlídál for his suggestions and advices. Furthermore I would like to thank to Ing. Pavel Nádaský for fruitful discussions and help in the laboratory. I also thank my parents for the financial support during studies.

Bc. Jakub Klus

CONTENTS

1	Introduction	3
2	Scattermeter II	5
2.1	Scanning procedure	5
2.2	Angular distribution of the scattered light intensity	6
2.3	New type of experiment	6
3	Mathematical description of the problem	9
3.1	Tammes's problem	9
3.2	Thomson's problem	9
3.3	Riesz's s-energy	10
4	Optimizing positions	11
4.1	Implementation of the steepest descent method	11
4.2	Parallelization of the procedure	13
4.3	Other approaches	16
5	Initial point configurations	17
5.1	Spiral points	17
5.2	Polyhedral breakdown systems	18
5.3	Parallel rings	23
6	Results	27
6.1	Polyhedral breakdown systems	27
6.2	Spiral points	37
6.3	Parallel rings	38
6.4	Repulsion forces	39
7	Applications	43
7.1	Visualizing spherical points	43
7.2	Generating the measurement sequence	45
8	Experiment	51
8.1	Time consumption	51
8.2	Angular distribution	52
8.3	Comparison with integrating sphere	53
9	Conclusions	55
10	Bibliography	57
11	List of symbols and abbreviations	59

1. INTRODUCTION

Since 2006 a device measuring an angular distribution of the light intensity scattered from a surface of solids had been developed in The Laboratory of Coherent Optics, IPE FME BUT. The basic purpose of the device was to verify simulations of the light scattering from studied surfaces, which were done within the framework of geometrical optics. This led to the quite extraordinary name of the device; Scattermeter. An original design from Gründling [1], nowadays called Scattermeter I (SM I), was complicated. Because of too many degrees of freedom the device was unable to repeat the same measurement conditions automatically. The construction itself had some disadvantages, namely a large shadowed area in the detector space and a high sensitivity to the ambient light.

An improved design came from the cooperation of Gründling and Brilla in 2009. New construction of the device is described in Brilla's master thesis [2], the device is familiarly called Scattermeter II (SM II). The ambient light was eliminated by housing the device into a lightproof box. Degrees of freedom were reduced to only two computer controlled coordinates. The light source was dismantled from the device and placed on an optical bench, to achieve exchangeability of various sources, which brought more measurement setups. The nearly completed device was ignored for more than a year, during this time all measurements were done on SM I. In 2011 a new master thesis was assigned to Nádaský focusing on measurements of solar cells by means of SM II.

Since Brilla left SM II unfinished, Nádaský has struggled with getting experimental results comparable with SM I. The whole process of finalizing SM II is described in his master thesis [3]. The main results are changes in the construction of the detector holder including the detector arm and the detailed description of setting up the experiment. Nevertheless the aim of [3] was not only to get the device running but also to classify certain solar cells provided by the company Solartec s.r.o. With samples provided, SM II was improved to determine the angular distribution of the light intensity scattered from the surface of solids as precisely as we believe is possible. The real capabilities are to be summarized in the next chapter of this work.

During the work of Nádaský on his thesis, there was an unanswered question: "Can we somehow compare our experimental results with other types of measurements?" Fortunately there are some measurements done directly on solar cells in Solartec s.r.o. using an integrating sphere enabling us to determine the energy scattered from the solar cell surface. When Nádaský finally received all the data he needed to compare performance of SM II with the integrating sphere, the results were completely different. After discussions in our laboratory we came to the conclusion that this difference can be caused by two main factors: a non-zero background signal on the detector and measuring in overlapping detector areas.

The aim of this work is to find a setup of non-overlapping detector area positions, so that the results acquired using SM II are directly comparable with the data measured by means of the integrating sphere. This should allow us to quantify the energy scattered in different directions. Another improvement is a reduction of the detector measurement positions which should result in a shorter acquisition time.

The next chapter is devoted to the current state of SM II, its capabilities, measurement process and problems which should be solved further in this thesis. Chapter 3 introduces the mathematical background of this thesis, basic definitions and approaches.

Chapter 4 describes a simple numerical method of optimizing detector positions. The following chapter shows three methods of generating non-overlapping detector setups, which are used in this work as initial setups. Further then in the sixth chapter the final tested configurations of detector positions are studied and their features are characterized. Chapter 8 is devoted to the application of the results on the measurement process of SM II. In the last two chapters we compare old and new measurement setups and then summarize the results of this work.

2. SCATTERMETER II

Scattermeter II (SM II) is a second generation of a unique device developed in The Laboratory of coherent optics, Institute of Physical Engineering, Faculty of Mechanical Engineering, Brno University of Technology. The main goal of it is to measure the angular distribution of the electromagnetic radiation scattered from the rough surfaces. Figure 2.1 illustrates the basic parts of SM II. The centre of the base plate determines the z-rotation axis (red dashed line). By rotating around this axis one can setup different incident angles of the source beam. The main motor unit, which moves the azimuth ring, is hidden inside the main stand, which is attached to the base plate with four screws.

The centre of the azimuth ring defines the azimuth rotation axis (blue dashed line). A sample is mounted in the holder, which can be extruded and tilted to align the normal of the sample with the azimuth rotation axis. The declination pivot consists of a holder and a declination motor which is placed on the azimuth ring. To ease the main motor unit load there is a counterweight on the opposite side of the ring. The declination motor shaft defines the declination axis (green dashed line).

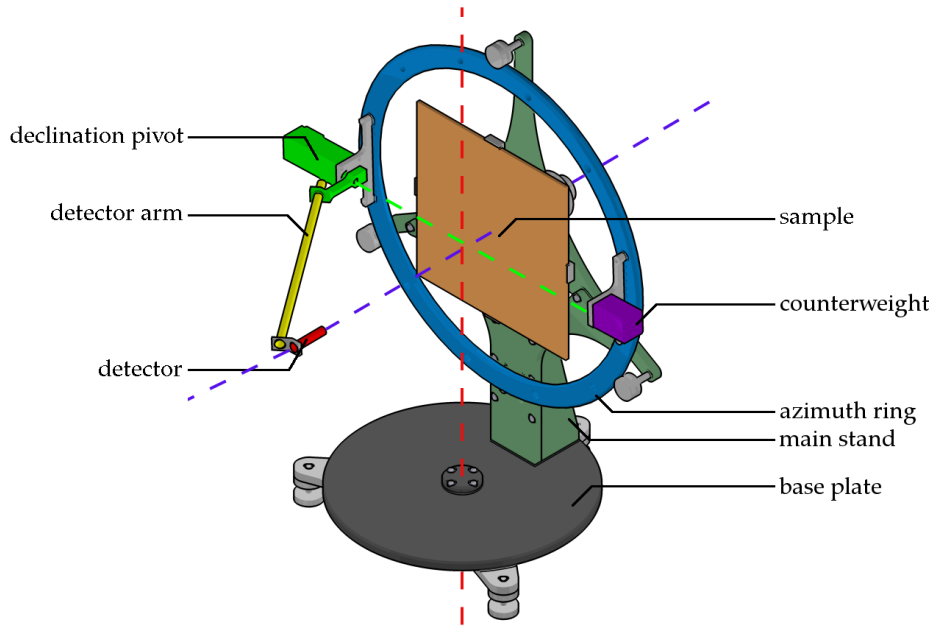


Figure 2.1: Schematic illustration of SM II without the source of radiation. There are three axes of rotation in the figure: z-rotation axis (red dashed line), azimuth rotation axis (blue dashed line) and declination axis (green dashed line). *Note: The centre of the sample is aligned with the rotation centre before each measurement.*

2.1. Scanning procedure

SM II is capable of measuring the scattered light intensity in discrete positions on a surface of a hemisphere. The positions are achieved by rotation around the azimuth and the declination axis with a constant radius. The radius of the hemisphere is determined by the detector arm length. Angular coordinates are not defined in the same way as it is usual for spherical coordinates in mathematics. Figure 2.2 shows that we

2.2. ANGULAR DISTRIBUTION OF THE SCATTERED LIGHT INTENSITY

define the azimuth angle ϕ from 0° to 180° and the declination angle θ from -90° to 90° , the declination 0° is on the pole of the hemisphere. Scanning starts by setting up the azimuth and the declination angle to the initial values. Then the declination angle increases by steps¹ towards the end position. In the last position of the declination angle the azimuth angle increases once and then the declination decreases towards the initial position. This repeats until the azimuth angle reaches its last position.

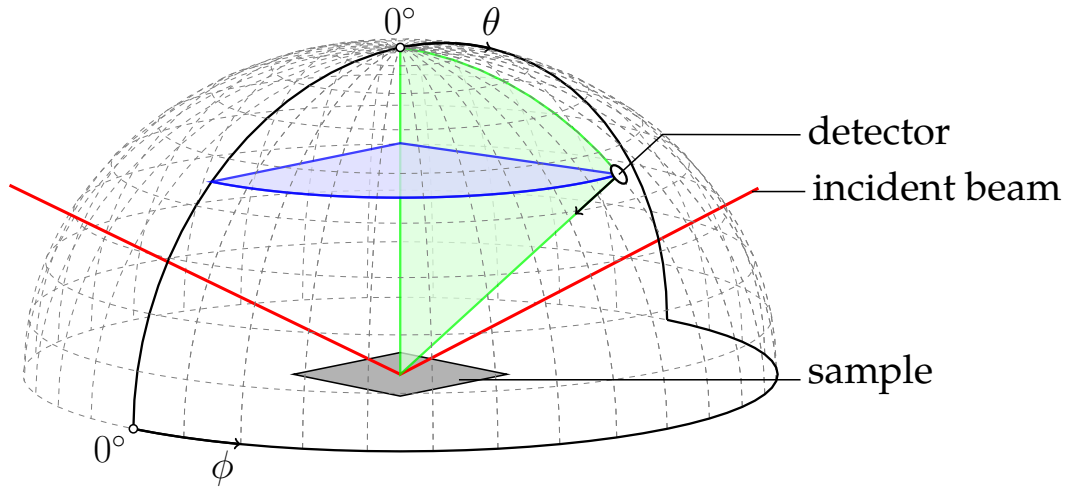


Figure 2.2: Modified hemispherical coordinates.

2.2. Angular distribution of the scattered light intensity

So far the best investigated measurement according to [3] is the angular distribution of the scattered light intensity. Using a red ($\lambda = 635 \text{ nm}$) laser source, SM II is capable of measuring the intensity of light reflected from a rough sample. From these results one can determine the main scattering directions for a certain sample. Rotation along the z -axis changes the incident angle of the laser beam.

SM II is also equipped with an infrared ($\lambda = 1550 \text{ nm}$) laser source. Current research is done on silicon solar cells, which are transparent for this laser. This allows us to also measure the angular distribution of the radiation transmitted through a rough sample. Unfortunately the construction of SM II does not allow us to change the angle of incidence for the transmission regime. Nevertheless with both the total transmission and the total reflection we can try to determine the energy trapped inside the solar cell as the difference between them. This new type of the measurement requires some data processing which is described in the next section.

2.3. New type of experiment

For angular measurements the actual values acquired from the device are not important. Because it was validated in [3] that the detector response is linear, we can nor-

¹This step also determines the resolution of the measurement, the best resolution is limited by the controlling software and the smallest step is 1° .

malize the distribution without influencing the results. Since we want to measure the total energy reflected and transmitted we need to convert the signal from photodiode to power and then integrate it over the whole hemisphere. As the first approximation we have summed the calibrated directional values. This led to the total power reflected from the sample greater than the power of the incident beam. We have found out that the problem was in overlapping of the detector positions. According to [2] the hemisphere radius is chosen in the way that detector's positions on the equator are touching each other. With a decreasing declination angle the detector positions become more and more overlapping. This can be compensated by multiplying the value measured with the detector by the ratio of the detector's active area and the area determined by the neighbouring detectors positions [3]. In this work we deal with a completely different approach, we will find a non-overlapping detector positions configuration with the maximal surface coverage. The next chapter deals with the mathematical definition of such a problem.

3. MATHEMATICAL DESCRIPTION OF THE PROBLEM

Although a grid of equidistant points in angular coordinates of the hemispherical system seems to be useful for the visualization, it is not applicable for integrating. Instead of a scanning detector let us consider an array of detectors¹. Setting up this array in the grid is not possible. So even if it is not the goal of this work, its results are also valid for constructing the Scattermeter as a static array of equivalent detectors.

To achieve better mathematical description we can consider not the hemispherical distribution, but the spherical one. Then we are searching for distribution of non-overlapping spherical caps with equal viewing angle on a surface of hemisphere. These problems are also referred as spherical packing problems.

3.1. Tammes's problem

The spherical packing problem is also referred as Tammes's problem [4]. Tammes was a Dutch botanist, who studied exit places on the surface of spherical pollen grains. The exit places on the surface of the pollen grain can be assumed to be circular caps of the same area. Tammes found out that the number of exits is related to the size of pollen grain and an area needed for one exit place [5]. The problem can be formulated as follows: "How many spherical caps of the same radius can be placed on a unit sphere without overlapping?" Another formulation is to find an arrangement of N points on a unit sphere that maximizes the minimum distance between any two of them. This is equivalent to the original Tammes's problem and also to our problem by thinking of the N points as the centres of spherical caps of an equal maximum radius.

3.2. Thomson's problem

A different approach for the similar problem was done by Sir Joseph John Thomson. In 1904 he proposed the model of the atom structure as follows: The atom is composed of electrons surrounded by a soup of positive charge to balance electron's negative charge. Thomson's problem concerns with position of electrons in a spherical atom shell and can be formulated in this manner: Find a minimum energy configuration of N electrons that repel each other with a force given by Coulomb's law on the surface of a sphere.

The more mathematical way to express this problem is: Let $\mathbf{r}_1, \mathbf{r}_2, \dots, \mathbf{r}_N$ be a collection of N distinct points on the unit sphere centred at the origin of the coordinate system. The energy of this configuration of points is defined to be:

$$\sum_{i < j} \frac{1}{|\mathbf{r}_i - \mathbf{r}_j|}. \quad (3.1)$$

Thomson's problem is to minimize this energy over all possible collections of N distinct points on the unit sphere.

¹ This layout was rejected because of the total cost and extremely complicated calibration of the detector array.

3.3. Riesz's s-energy

The bridge between Tammes's problem and Thomson's problem is Riesz's s -energy. The Riesz's energy is called after M. Riesz, who derived a number of important properties of Riesz potentials [6]. For a collection of $N \geq 2$ distinct points $X_N = \{\mathbf{x}_1, \dots, \mathbf{x}_N\}$ and $s > 0$, the discrete Riesz's s -energy of X_N is defined by:

$$E_s(X_N) = \sum_{j \neq k} \frac{1}{|\mathbf{x}_j - \mathbf{x}_k|^s}. \quad (3.2)$$

Searching for the minimal E_s , when $s = 1$ and N is fixed we are solving Thomson's problem. On the other hand when $s \rightarrow \infty$ and N is fixed, we get the best packing problem, which is the problem of finding N -point configuration with the largest separation radius [7].

From the solution of best packing problems in the plane, one can expect that the best solution for the spherical surface will consist of hexagons [8]. But according to Euler's characteristic²: $F - E + V = 2$, where F is the number of faces, E is the number of edges and V is the number of vertices, sphere cannot be tiled only using hexagons. Let us suppose that sphere will be divided using only hexagons and pentagons. Assuming that exactly 3 edges originate from each vertex it follows from Euler's characteristic that there has to be exactly 12 pentagons in order to fit on the sphere [8].

A common way to solve the best packing problem is based on numerical optimization using a computer, but with growing number of points the problem starts to be very challenging. Largest list of spherical codes is provided on <http://neilsloane.com/>. The author of the web is also co-author of [9] where the packing problem is described by means of mathematics. Computations uncovered that there are many local minima for the s -energy problem, which are not global minima, but their energies are very close to the global minimum [8]. It is estimated that the number of distinct local minima grows exponentially with N . This is one of the reasons why the packing problem can be used for testing the global optimizing methods [8].

²Euler's characteristic is an topological invariant which is for the case of a convex polyhedron (sphere) equal to 2 [8].

4. OPTIMIZING POSITIONS

In this chapter we will introduce the numerical optimizing method for finding a minimum of the s -energy. There are many optimization methods, but as the first approach most commonly used is the steepest descent method [4, 10] as the basic and simple method [11].

The steepest descent (gradient) method is a first-order optimization algorithm. Let us have a function of n variables $f(x_1, \dots, x_n)$ which is differentiable on \mathbb{R} (for convenience we will write $\mathbf{x} = (x_1, \dots, x_n)$ and $f(\mathbf{x})$ in vector notation). The idea of this method is to find a minimum of $f(\mathbf{x})$ by repeatedly computing minima of a function $g(t)$ of a single variable t [12]. Suppose that $f(\mathbf{x})$ has a minimum at \mathbf{X}_0 and we are starting at a point \mathbf{x}_1 . Then in the first step we search for a minimum of $f(\mathbf{x})$ along the straight line in the direction of $-\nabla|_{\mathbf{x}_1} f(\mathbf{x})$, which is closest to \mathbf{X}_0 . We change the \mathbf{x} starting from the point \mathbf{x}_1 by the step $-t_1 \cdot \nabla|_{\mathbf{x}_1} f(\mathbf{x})$:

$$\mathbf{z}(t) = \mathbf{x} - t_1 \nabla|_{\mathbf{x}_1} f(\mathbf{x}). \quad (4.1)$$

To find t_1 we minimize the function:

$$g(t) = f(\mathbf{z}(t)). \quad (4.2)$$

At the minimum of $g(t)$, $\mathbf{z}(t)$ is closest to \mathbf{X}_0 , so we take $\mathbf{z}(t_1)$ in the next step as a start point \mathbf{x}_2 . The optimization process is stopped when changes of subsequent t_i are small enough.

4.1. Implementation of the steepest descent method

In our case the steepest descent method comes from the physical background of the problem. We assume a set of N points and their position vectors $\mathbf{r}_1, \dots, \mathbf{r}_N$. Let us define scalar potential of the i -th point $\varphi_i(\mathbf{r})$ as follows:

$$\varphi_i(\mathbf{r}) = Q \cdot \frac{1}{|\mathbf{r} - \mathbf{r}_i|^s}, \quad (4.3)$$

where \mathbf{r} is a position in \mathbb{R}^3 , s defines the potential (see Chapter 3) and Q is an arbitrary constant. The direction of a steepest descent is:

$$-\nabla\Phi(\mathbf{r}, \mathbf{r}_1, \dots, \mathbf{r}_N) = \mathbf{F}(\mathbf{r}, \mathbf{r}_1, \dots, \mathbf{r}_N), \quad (4.4)$$

where $\mathbf{F}(\mathbf{r}, \mathbf{r}_1, \dots, \mathbf{r}_N)$ is the net force and $\Phi(\mathbf{r}, \mathbf{r}_1, \dots, \mathbf{r}_N)$ is the total potential in the position \mathbf{r} given by the equation:

$$\Phi(\mathbf{r}, \mathbf{r}_1, \dots, \mathbf{r}_N) = \sum_{i=1}^N \varphi_i(\mathbf{r}) = Q \cdot \sum_{i=1}^N \frac{1}{|\mathbf{r} - \mathbf{r}_i|^s} \quad (4.5)$$

The value of $-\nabla\Phi(\mathbf{r}, \mathbf{r}_1, \dots, \mathbf{r}_N)$ can be determined numerically by evaluating all the partial derivatives of $\Phi(\mathbf{r}, \mathbf{r}_1, \dots, \mathbf{r}_N)$ for all components using for example the finite difference approximation:

$$\frac{\partial\Phi}{\partial x_i} = \frac{\Phi(x, x_1, \dots, x_i + h, \dots, x_N) - \Phi(x, x_1, \dots, x_i, \dots, x_N)}{h}, \quad (4.6)$$

4.1. IMPLEMENTATION OF THE STEEPEST DESCENT METHOD

$$\frac{\partial \Phi}{\partial y_i} = \frac{\Phi(y, y_1, \dots, y_i + h, \dots, y_N) - \Phi(y, y_1, \dots, y_i, \dots, y_N)}{h}, \quad (4.7)$$

$$\frac{\partial \Phi}{\partial z_i} = \frac{\Phi(z, z_1, \dots, z_i + h, \dots, z_N) - \Phi(z, z_1, \dots, z_i, \dots, z_N)}{h}, \quad (4.8)$$

where $h \rightarrow 0$ is the step of differentiation. This process involves $4N$ calculations of $\Phi(\mathbf{r}, \mathbf{r}_1, \dots, \mathbf{r}_N)$ and every calculation of $\Phi(\mathbf{r}, \mathbf{r}_1, \dots, \mathbf{r}_N)$ requires N calculations of $\varphi_i(\mathbf{r})$. This can lead to a very intensive usage of computing power. However, we can avoid calculating $-\nabla \Phi(\mathbf{r}, \mathbf{r}_1, \dots, \mathbf{r}_N)$ numerically by just expressing the explicit equation for net force $\mathbf{F}(\mathbf{r}, \mathbf{r}_1, \dots, \mathbf{r}_N)$. From the equation (4.3) we can derive the formula for the force caused by the i -th point $\mathbf{F}_i(\mathbf{r})$ analytically:

$$\mathbf{F}_i(\mathbf{r}) = Q_1 \cdot \frac{\mathbf{r} - \mathbf{r}_i}{|\mathbf{r} - \mathbf{r}_i|^{s+2}}, \quad (4.9)$$

where Q_1 is arbitrary constant. Then the net force $\mathbf{F}(\mathbf{r}, \mathbf{r}_1, \dots, \mathbf{r}_N)$ of the set $\mathbf{r}_1, \dots, \mathbf{r}_N$ in the position \mathbf{r} can be estimated as a vector sum of all N forces caused by points of our set:

$$\mathbf{F}(\mathbf{r}, \mathbf{r}_1, \dots, \mathbf{r}_N) = \sum_{i=1}^N \mathbf{F}_i(\mathbf{r}) = Q_1 \cdot \sum_{i=1}^N \frac{\mathbf{r} - \mathbf{r}_i}{|\mathbf{r} - \mathbf{r}_i|^{s+2}} = -\nabla \Phi(\mathbf{r}, \mathbf{r}_1, \dots, \mathbf{r}_N). \quad (4.10)$$

According to equation (3.2) we define the energy of our system of N particles $X_N = \{\mathbf{r}_1, \dots, \mathbf{r}_N\}$ as follows:

$$E_s(X_N) = \sum_{j \neq k} \frac{1}{|\mathbf{r}_j - \mathbf{r}_k|^s} = \sum_{j>0}^N \sum_{k>0, k \neq j}^N \varphi_k(\mathbf{r}_j). \quad (4.11)$$

The direction of the steepest descent for i -th point is then equal to the net force $\mathbf{F}_{i,\text{net}}$ acting on the i -th point:

$$\mathbf{F}_{i,\text{net}} = Q_1 \sum_{j=1, j \neq i}^N \frac{\mathbf{r}_j - \mathbf{r}_i}{|\mathbf{r}_j - \mathbf{r}_i|^{s+2}}. \quad (4.12)$$

After determining the forces $\mathbf{F}_{i,\text{net}}$ we search for a new system of particles $X'_N = \{\mathbf{r}'_1, \dots, \mathbf{r}'_N\}$ which fulfil:

$$\mathbf{r}'_i = \mathbf{r}_i + t \cdot \mathbf{F}_{i,\text{net}}, \quad (4.13)$$

where t is changed until $E_s(X'_N) > E_s(X_N)$. The algorithm works with the Cartesian coordinate system in Euclidean space \mathbb{R}^3 . It can be described in eight steps:

1. Let us have an initial set of N points $X_N = \{\mathbf{r}_1, \dots, \mathbf{r}_N\}$ on a unit sphere and an initial value of t . Calculate the s -energy $E_s(X_N)$.
2. Calculate the net force $\mathbf{F}_{i,\text{net}}$ acting on each point.
3. Subtract the normal component from the net force.
4. Calculate set of points $X'_N = \{\mathbf{r}'_1, \dots, \mathbf{r}'_N\}$, according to (4.13).
5. Normalize vectors $\mathbf{r}'_1, \dots, \mathbf{r}'_N$.

6. Calculate the energy $E_s(X'_N)$.
7. If $E_s(X'_N) > E_s(X_N)$ decrease the value of t and continue with step 4.
8. If $E_s(X'_N) < E_s(X_N)$ use the X'_N as a new value of X_N and continue with step 2.

Steps 3 and 5 are important for keeping the points on the unit sphere. Normalization in step 5 is straightforward. All vectors with the same length are on the same spherical surface. As it is depicted in Figure 4.1, subtracting the normal component $\mathbf{F}_{i,n}$ from the net force $\mathbf{F}_{i,\text{net}}$ gives us a direction in the tangential plane $\mathbf{F}_{i,t}$ which has better confinement to the unit sphere surface.

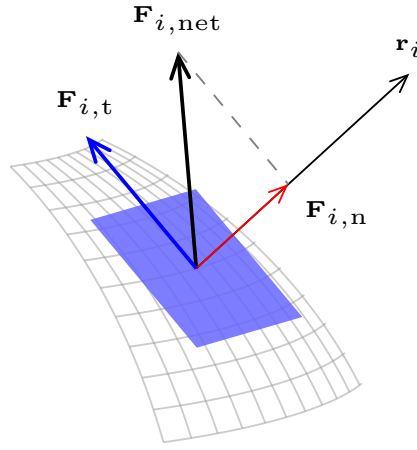


Figure 4.1: Illustration of the subtraction of the normal component $\mathbf{F}_{i,n}$ from the net force $\mathbf{F}_{i,\text{net}}$. The resulting vector $\mathbf{F}_{i,t}$ is lying in the blue tangential plane of the sphere.

4.2. Parallelization of the procedure

The optimization procedure described above has quadratic complexity $\mathcal{O}(n^2)$, the number of calculations can be reduced to half. In the case of calculating the energy $E_s(X_N)$, we can use the fact that the potential is symmetric and is a function only of the mutual distance:

$$\varphi_i(\mathbf{r}_j) = C \cdot \frac{1}{|\mathbf{r}_j - \mathbf{r}_i|^s} = C \cdot \frac{1}{|\mathbf{r}_i - \mathbf{r}_j|^s} = \varphi_j(\mathbf{r}_i). \quad (4.14)$$

Then the s -energy of the system $E_s(X_N)$ can be evaluated by only half the additions:

$$E_s(X_N) = 2 \cdot \sum_{j>0}^N \sum_{k>j}^N \varphi_k(\mathbf{r}_j). \quad (4.15)$$

To achieve the same performance for calculating the net force we can use Newton's third law: "The forces of two bodies on each other are always equal and are directed in

4.2. PARALLELIZATION OF THE PROCEDURE

opposite orientation." There is no simple formula to prove the impact on the procedure, but when we calculate the force that the j -th point is acting on the i -th point we can store it also as an opposite force of the i -th point acting on the j -th and do not evaluate it again:

$$\mathbf{F}_j(\mathbf{r}_i) = C_1 \sum_{j=1, j \neq i}^N \frac{\mathbf{r}_i - \mathbf{r}_j}{|\mathbf{r}_i - \mathbf{r}_j|^{s+2}} = -\mathbf{F}_i(\mathbf{r}_j) = -C_1 \sum_{j=1, j \neq i}^N \frac{\mathbf{r}_i - \mathbf{r}_j}{|\mathbf{r}_i - \mathbf{r}_j|^{s+2}}. \quad (4.16)$$

Although we have halved the total number of calculations we still have to deal with an enormous number of operations. This is the reason why we have implemented the algorithm in programming language C for parallel computers¹. We will not discuss the implementation here, but we will illustrate how the work is distributed between workers to shorten the time needed for the one iteration of the optimization.

Because the load distribution process is the same for both the energy and the net force computation we will show it only for the energy. Assume that we have w workers and a set of N points (we treat the point as a task which has to be solved by a worker). To calculate the i -th point contribution we have to evaluate (4.3) $(N - i)$ times, the total number of calculations is then $n = \frac{N(N-1)}{2}$, please note that last point has no other to interact with, so we actually have to distribute only $N-1$ tasks. The first approach is to assign the same number of tasks w_i to each worker. In principle it is not exactly possible, so we have assigned $\lfloor \frac{N-1}{w} \rfloor$ tasks to the first $w - 1$ workers and the rest to the last worker.

Let us demonstrate the distribution on the example of 30 points and 6 workers. We have assigned four tasks to each of first five workers and then the remaining ten tasks to the last one. As we can see in Figure 4.2, the first worker is doing more than twice

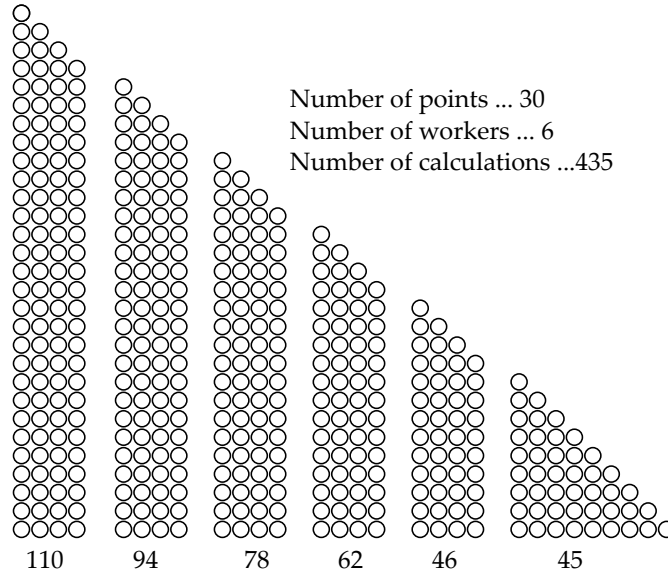


Figure 4.2: Distributing calculations of 30 points among 6 workers. Each worker, except the last one, has the same range of points. The number below the pile denotes the sum of calculations performed by the worker.

¹Our laboratory is equipped with a grid of 7 computers with the total count of 28 processors. The parallelization was done using the Message Passing Interface (MPI) protocol.

the number of calculations performed by the last worker. In general, the number of calculations performed by each worker is varying. This is caused by the fact that low-numbered tasks consist of a huge number of calculations. In the actuality there were 28 workers and roughly 35000 points, so each worker was assigned 1249 tasks. First worker is calculating approximately 43.0 million calculations, but the last worker only 0.8 million calculations from the total sum of 612.5 million calculations.

The procedure described above is not distributing the load equally among the workers. To achieve better efficiency we should focus on partitioning the number of calculations rather than the number of tasks. This approach requires matching the k -th calculation to the corresponding task i . This relation can be obtained using:

$$i = \left\lceil \frac{2N-1}{2} - \sqrt{\left(\frac{2N-1}{2}\right)^2 - 2k} \right\rceil. \quad (4.17)$$

The equation (4.17) can be derived from relations valid for the arithmetic progression [6]. Figure 4.3 illustrates the new load distribution procedure again on the example of 30 points and 6 workers. The ratio of the numbers of calculations performed by the first

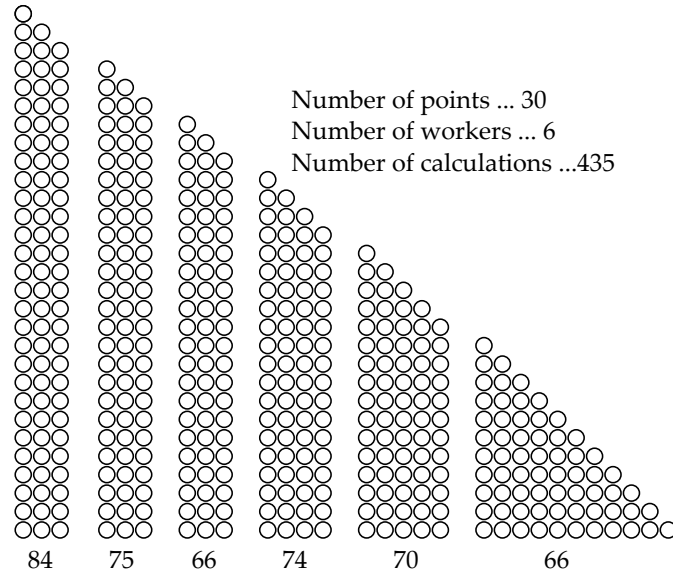


Figure 4.3: Improved load distribution of calculations of 30 points among 6 workers. The number below the pile denotes the sum of calculations performed by the worker, variation between numbers of calculations assigned per worker is lower.

and the last worker is significantly lower. The load is more balanced. In practice the number of calculations is proportional to the CPU time consumed. In the first case the last worker is waiting for the first one to finish his assignment most of its time. In the second case all workers finish almost simultaneously. This fact can be better viewed in the actuality, where the first worker performed 21 919 972 and the last one 21 988 396 calculations. We can clearly see that the ratio of the number of calculations assigned to the first and the last worker significantly changes from 53.750 in the first case to 0.996 in the second case.

4.3. Other approaches

In this section we want to discuss some approaches that were rejected during the work on this thesis, mainly because of the possible instability of the system or poor computational performance. Optimizing algorithm will work for any potential $\varphi(r)$, where r is the mutual distance of points, where the force $\mathbf{F}(r)$ can be analytically derived. We tried the Lennard-Jonnes potential:

$$\varphi(r) = \varepsilon \left[\left(\frac{r_m}{r} \right)^{12} - \left(\frac{r_m}{r} \right)^6 \right], \quad (4.18)$$

where r_m and ε are arbitrary constants. The r^{-12} term describes repulsion and r^{-6} attraction. The force acting on a particle is zero at distance r_m and the potential is $-\varepsilon$. This approach was rejected because the attractive part caused the particles to form clusters, where the distances inside the cluster were shortened by repulsive forces of the surrounding particles, which were bound together by the attractive force.

Another approach was with the linear spring potential:

$$\varphi(r) = \frac{1}{2}kr^2, \quad (4.19)$$

where k is so-called spring constant. Unfortunately the equilibrium state of even number of points on a spherical surface is half of the points on one pole and half on the opposite pole.

Assuming that we determine the net force acting on each particle, we do not necessarily need to use it as a gradient of a potential energy of the configuration. We can use Newtonian mechanics and define the velocity and the acceleration of a point. To simulate a classical mechanic problem we have to use far more complicated procedures, like Runge-Kutta method. Such a methods use four times more calculations per iteration because of the overall progress predictions. Another problem with the mechanical system is that particles forming clusters are accelerated more, which results in their higher velocity. With inhomogeneous distributions local clusters can emit points with significantly higher velocity. To avoid such behaviour, we should include the viscosity factor, which would not allow the point to travel over the surface infinitely. On the other hand it prevents the system from oscillating.

Briefly the energy optimization is straightforward; we only accept configurations with the lower energy, in contrary with mechanics where we would accept configurations with low speeds (stable configuration). Nevertheless the s -energy strongly diverges for $r \rightarrow 0$ that means for nearly identical points. To avoid this problem, we have searched and implemented three algorithms which can generate better initial configuration then just random positioning on the spherical surface. These algorithms are explained in the next chapter.

5. INITIAL POINT CONFIGURATIONS

As it was mentioned in the previous chapter, because of divergence of $\varphi(\mathbf{r})$ we have to assure that the initial configuration for the optimizing algorithm will not contain identical (duplicate) points. We can do that by either controlling the random positions generated, or by creating the initial point configuration more wisely. Uniformly distributing a set of points on a surface of a sphere is a complicated problem. In the sections below there are three methods of generating initial configurations explained, which have the desired features.

5.1. Spiral points

According to their previous work on numerical simulations [13] Rahkmanov, Saff, and Zhou in [8] introduced construction, which provides sufficiently uniform distribution of N points on a spherical surface. In spherical coordinates $\theta \in \langle 0, \pi \rangle$ and $\phi \in \langle 0, 2\pi \rangle$ we can define the k -th point as follows:

$$\theta_k = \arccos(h_k), h_k = -1 + \frac{2(k-1)}{(N-1)}, \text{ for } 1 \leq k \leq N, \quad (5.1)$$

$$\phi_k = \left(\phi_{k-1} + \frac{3.6}{\sqrt{N}} \frac{1}{\sqrt{1-h_k^2}} \right) (\bmod 2\pi), \text{ for } 2 \leq k \leq N-1, \quad (5.2)$$

$$\phi_1 = \phi_N = 0. \quad (5.3)$$

Such a set of points is called a generalized spiral set [8]. The variable h_k is z -coordinate

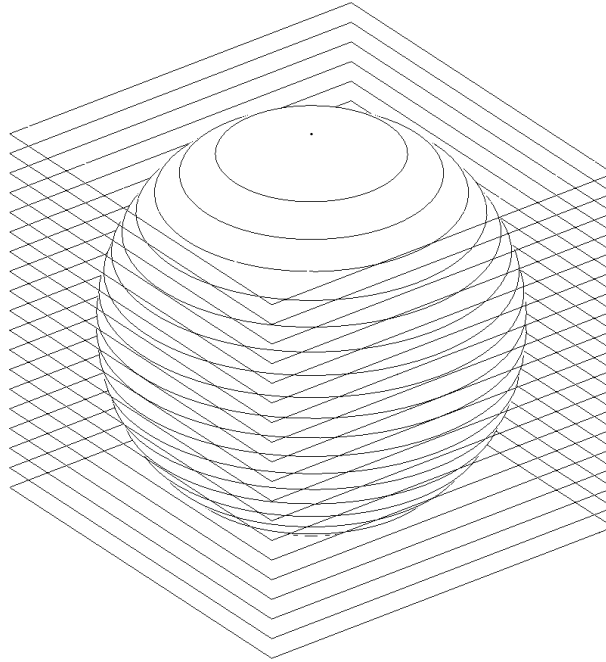


Figure 5.1: Cutting a unit sphere with 20 horizontal planes.

of the k -th point. The term $\frac{3.6}{\sqrt{N}}$ is a constant chosen by Rahkmanov, Saff and Zhou, based on their experience with numerical simulations of spherical arrangements. In

5.2. POLYHEDRAL BREAKDOWN SYSTEMS

fact the value should be roughly $\left(\frac{8\pi}{\sqrt{3}}\right)^{1/2} \cdot \frac{1}{\sqrt{N}} \approx \frac{3.809}{\sqrt{N}}$, which is an equation derived by Habicht and van der Waerden [14] who dealt with asymptotic solutions of Tammes's problem [8].

Geometrical interpretation of the generalized spiral set explains the procedure more intuitively. Let us cut the unit sphere with N horizontal planes with mutual spacing $\frac{2}{N-1}$. As it is shown in Figure 5.1, intersections with the spherical surface are circles with centres on the z axis. The first and the last circle are degenerated circles without the diameter forming the north and the south pole. Each circle contains exactly one point, starting with the first point on the south pole one moves upwards in the elevation to the next circle and then counter-clockwise in the azimuth for a fixed distance to arrive at the next point. An example of this construction is shown in Figure 5.2, where the generalized spiral set is generated for 20 points.

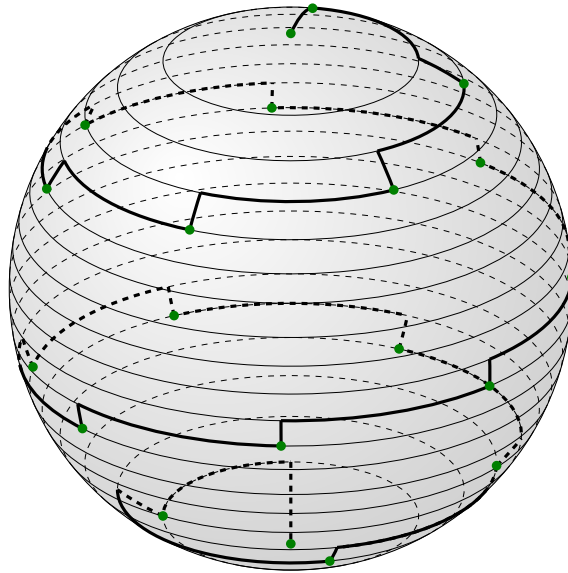


Figure 5.2: Generalized spiral set for 20 points.

5.2. Polyhedral breakdown systems

Another approach is to take a convex polyhedron inscribed in a unit sphere and divide its faces. The division of the faces forms points which are then projected back on the unit sphere. The methods of polyhedron subdivisions are well described by Clinton in his technical report for NASA [15]. Terminology used by Clinton is now a common way of describing the phenomena in this field, called geodesic geometry or geodesic math [16]. All spherical coordinate systems described in the previous sections used the common way of representing position vectors on a unit sphere by using two angular coordinates (θ, ϕ) . The comparison of the sphere division between the spherical coordinate system and the polyhedral system is shown in Figure 5.3.

To achieve better uniformity we do not want to deal with a generic polyhedron. A suitable class of polyhedrons are Platonic solids. They are regular and convex. Regular means that the polyhedron consists of identical polygons. There are five Platonic

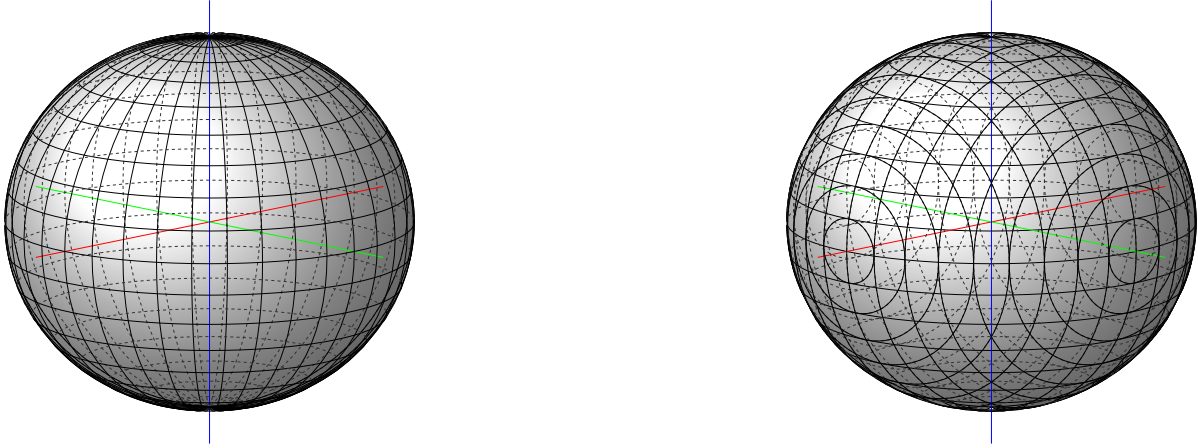


Figure 5.3: Schematic representation of the difference between the sphere division in spherical coordinates (left) and the polyhedral system (right).

solids: the tetrahedron, the hexahedron (cube), the octahedron, the dodecahedron and the icosahedron.

We are focusing on the tetrahedron, the octahedron and the icosahedron, because they are made of equilateral triangular faces (the hexahedron is made of squares and the dodecahedron is made of equilateral pentagons). Before introducing the subdivision methods, let us describe the polyhedrons and their features. The last thing to mention is that we will use the term frequency ν which is the number of segments that we divide the edge into.

The tetrahedron consists of four vertices, six edges and four faces. Its model is in Figure 5.4. Its main disadvantage is that to achieve the same number of points on the unit sphere, the tetrahedron has to be subdivided more. The higher subdivision frequency results in the higher variation of mutual distances. Another problem is the absence of the equator.

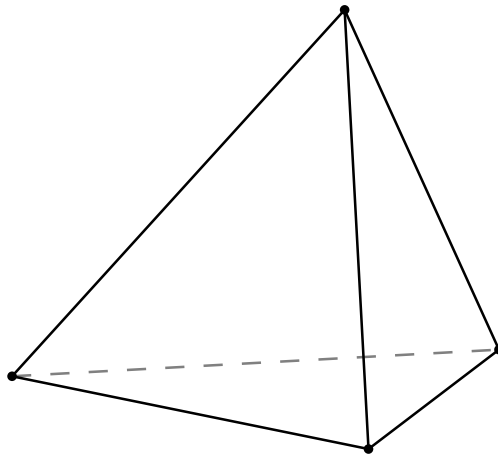


Figure 5.4: Schematic plot of the tetrahedron.

The octahedron is shown in Figure 5.5. It consists of six vertices, twelve edges and eight faces. In contrary with the tetrahedron it has a natural equator for all frequencies

5.2. POLYHEDRAL BREAKDOWN SYSTEMS

[16] which allows us to divide it into hemispheres (domes). Other features are more of architectural importance. Firstly the vertical slicing is useful for hemispheres to be joined to rectangular structures. Secondly the octahedron is useful for generating non-spherical (ellipsoidal) contours. The multipole system in Figure 5.3 has the octahedral symmetry.

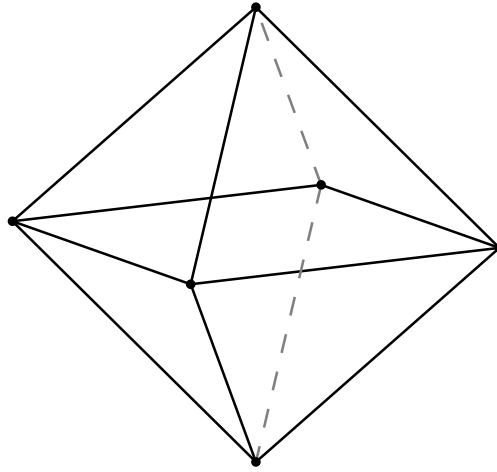


Figure 5.5: Schematic model of the octahedron.

The icosahedron is defined by twelve vertices, two of them are poles and ten vertices are aligned in two pentagons rotated against each other, vertices of pentagons are emphasized with the same color in Figure 5.6. The icosahedron has twenty faces

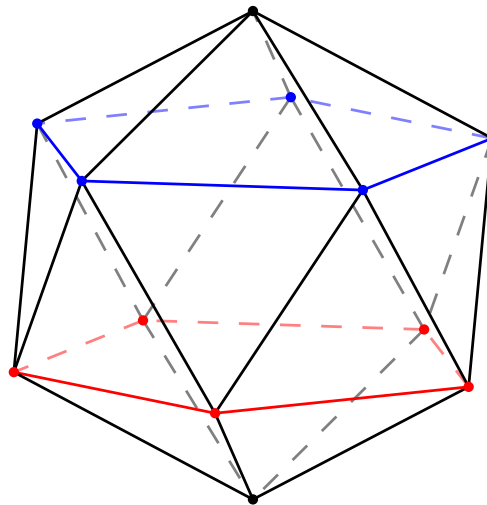


Figure 5.6: Illustration of the icosahedron with emphasized vertices and edges forming the upper and the lower pentagon.

and thirty edges. The main advantage of it is that its faces are close to the spherical

5. INITIAL POINT CONFIGURATIONS

surface and the mutual point distance variation is the lowest of the three polyhedrons discussed. The natural equator is only available for even frequencies.

When describing subdivision methods we will be concerned only with one triangle of the polyhedron called the principal polyhedral triangle (PPT). Since triangles are equivalent, constructing subdivision on others is only a matter of a transformation.

In the first method (method 1) the PPT is divided with the frequency ν by equidistant divisions along the triangle sides. Each point is then connected with a line parallel to the respective side. This forms a grid of equilateral triangles. The created points are then translated along a line, connected with the origin of the coordinate system O, to the surface of the circumscribed sphere. This process is illustrated in Figure 5.7.

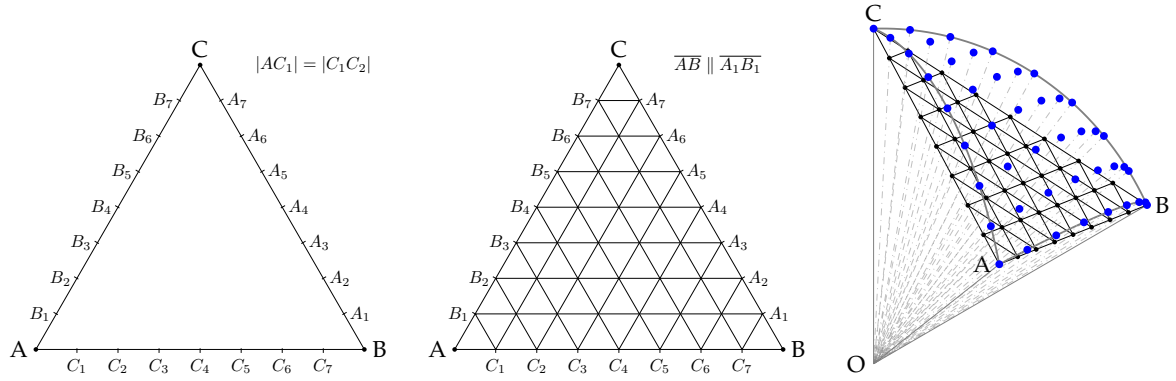


Figure 5.7: Process of creating a subdivision using method 1.

Method 2 subdivides the PPT side into ν parts that correspond to equal arc divisions on the circle formed as an intersection with circumscribed sphere. Each point is then connected with a line parallel to the respective side. Because of the method of the subdivision the parts on the PPT side are not equal. The created grid has many points of intersection. As it is shown in Figure 5.8, these intersections form small triangles. The centres of them are again translated along the line connected with origin O to the surface of the circumscribed sphere.

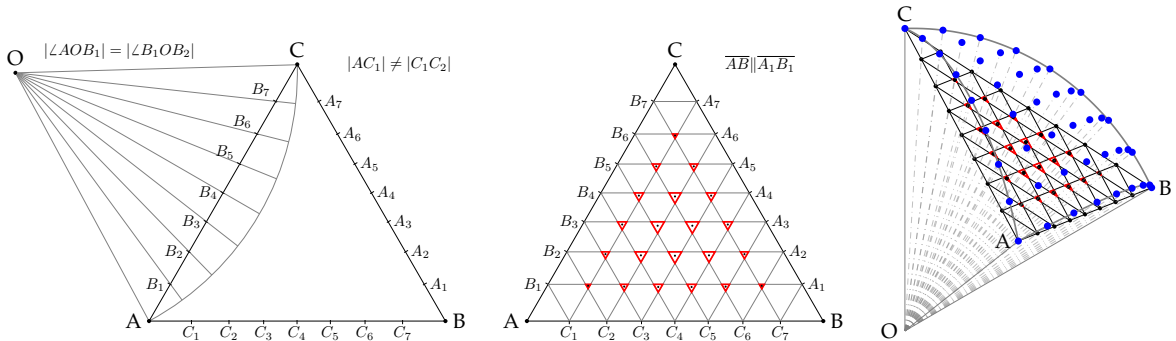


Figure 5.8: Subdivision using method 2. The side division is depicted on the left side. The formation of triangular windows can be seen in the middle. Finally the projection to the unit sphere surface is sketched on the right.

The third method (method 3) divides the PPT into the frequency ν with equal parts along the triangle sides. But in this method each point of the respective side is con-

5.2. POLYHEDRAL BREAKDOWN SYSTEMS

ected with every corresponding second point of the remaining sides. Lines connecting points are perpendicular to the respective side. The formed grid of points is then translated onto the surface of the circumscribed sphere along the line connected with origin O. Figure 5.9 shows the triangular grid.

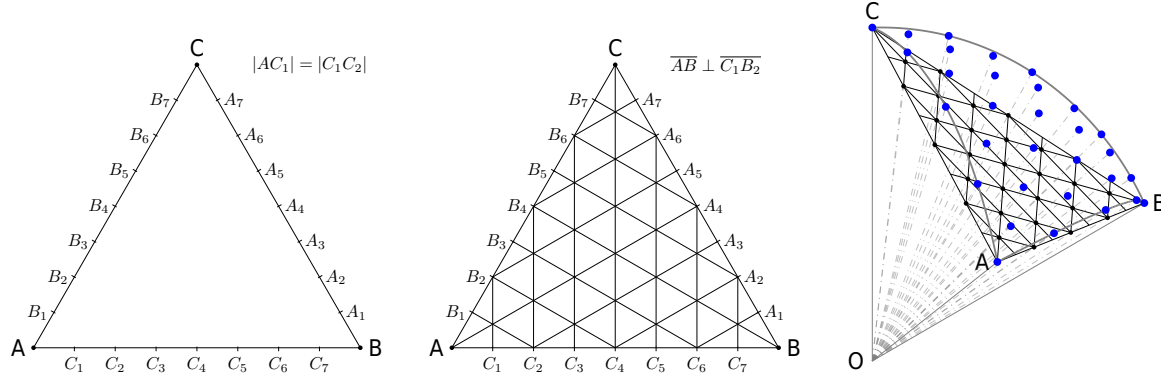


Figure 5.9: Triangular grid created using method 3.

The last method (method 4) described in this work subdivides PPT into the frequency ν with parts that correspond to equal arc divisions. Each point is connected in the same way as in method 3, but lines are not perpendicular to their respective sides. This subdivision again causes small triangles to occur. Their centres are translated to the surface of the circumscribed sphere in the same way as in the previous methods. The resulting PPT subdivision is depicted in Figure 5.10.

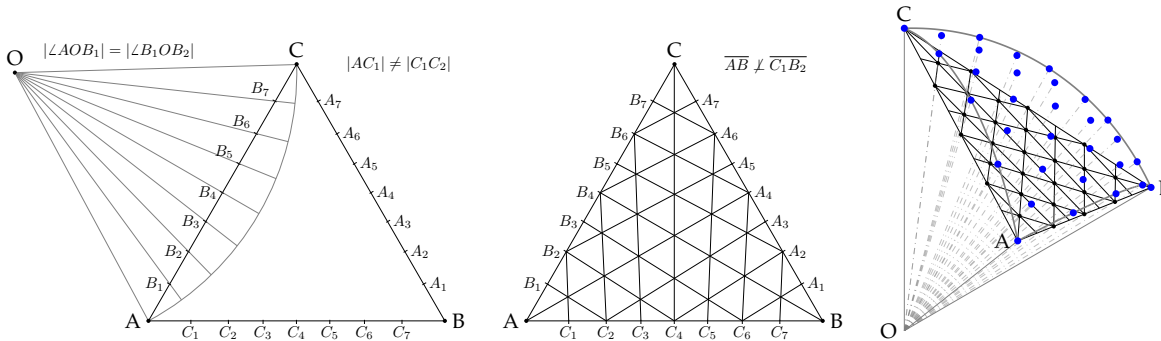


Figure 5.10: Triangle subdivision according to method 4. Note that triangular windows are too small (see Figure 5.8) and are not coloured. One can clearly see that the subdivision lines are not parallel to the respective sides.

There are seven methods described in [15]. We have introduced only those which seemed to be applicable for us. The terminology from [15] was renewed in [16]. There methods 1 and 2 belong to so-called Class I (Alternate) subdivision and methods 3 and 4 belong to Class II (Triacon) subdivision. The difference between Class I and Class II is emphasized in Figure 5.11. Apart from the visual difference there is also a practical one. Class II subdivisions can only be generated for odd frequencies.

The multipole system in Figure 5.3 has the octahedral symmetry and represents method 2 (Class I) breakdown system with the frequency $\nu = 9$.

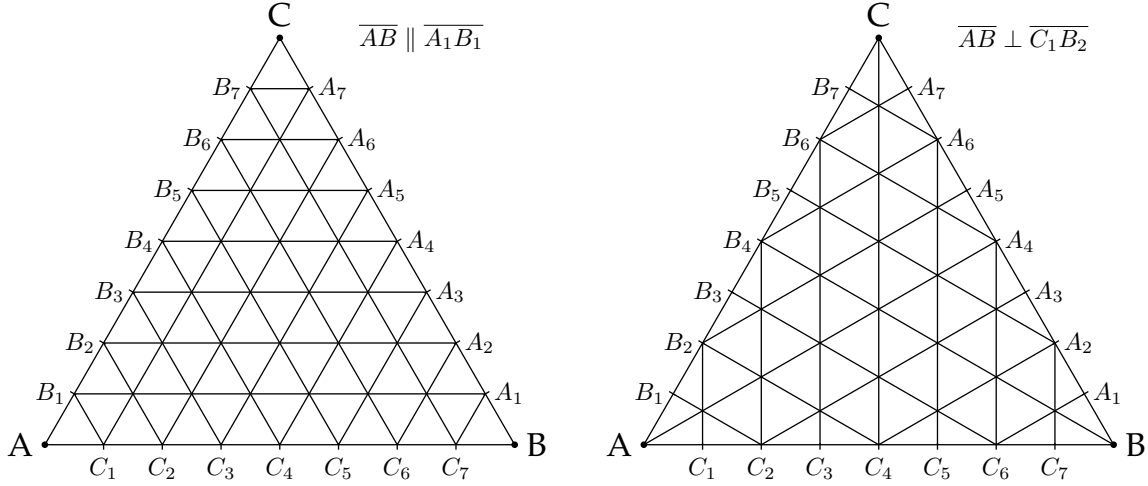


Figure 5.11: Division of the principal triangle. There is Class I (Alternate) subdivision on the left and Class II (Triacon) on the right. Principal triangle illustrations are taken from methods 1 and 3.

5.3. Parallel rings

This principle was introduced by Appelbaum and Weiss [17]. After a short discussion with Prof. Appelbaum we found out that a hemispherical spatial irradiation measuring system was constructed on the basis of his previous papers [18]. Parallel rings principle was originally designed for the arrangements of N equal detectors on a hemisphere¹ of a radius R . Each detector is a circle (spherical cap) characterized by the angles α_i, γ_i and η . These angles are illustrated in Figure 5.12, α_i is the elevation angle with respect to the equatorial plane of the hemisphere, γ_i is the detector azimuth distance from a reference direction and η is the viewing angle. The problem is extended by detectors with varying viewing angle η_i , since its solution is also a solution for the case of equal detectors.

There are some assumptions for practical reasons:

- The detectors are arranged in concentric circles² (rings) on the surface of the hemisphere.
- The detectors in the same ring have the same viewing angles.
- The detectors are equally distributed on the each ring circumference.
- The elevation angle between two successive rings is equal to the sum of the viewing angles of two detectors.

The solution of the problem starts with defining the arrangement of the detectors. This means that the number of rings C and the number of detectors in each ring n_c must

¹The hemisphere can be transformed to the sphere by reflecting all points by the equatorial plane to fit better into mentioned spherical distributions.

²From this assumption the term "Parallel ring" comes. The name is only used for purposes of this thesis to distinguish different approaches for distributing points on a spherical surface.

5.3. PARALLEL RINGS

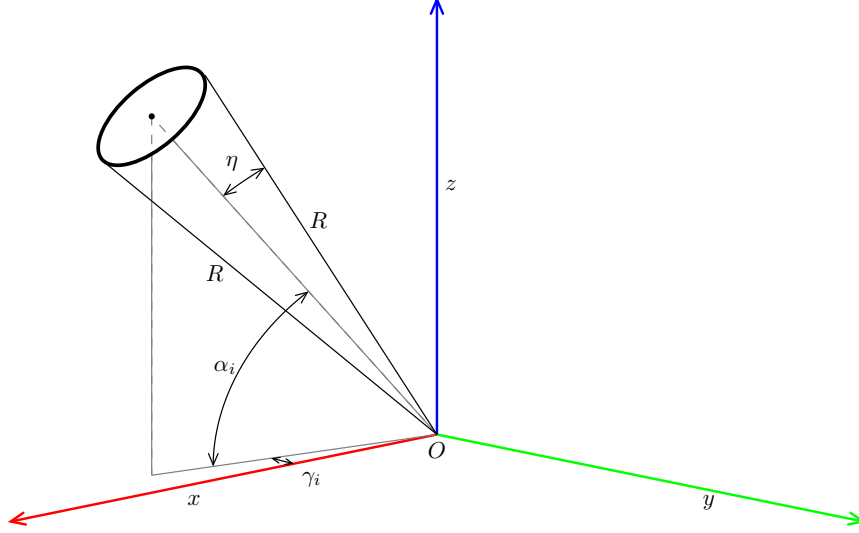


Figure 5.12: Schematic illustration of angles defined for the detector (spherical cap).

be selected. For given number of detectors N , there can be many possible arrangements. The number of detectors for the respective arrangement can be calculated as $N = \sum_{c=1}^C n_c$. Now we need to find the elevation α_c and viewing angle η_c of detectors placed in the c -th ring satisfying all the assumptions we made. We start with the lowest circle and move upwards circle by circle. We can express the elevation of c -th ring with the elevation and the viewing angle of the ring $c - 1$:

$$\alpha_c = \alpha_{c-1} + \eta_{c-1} + \eta_c. \quad (5.4)$$

The only unknown quantity is the viewing angle of the current ring η_c . The arc angle

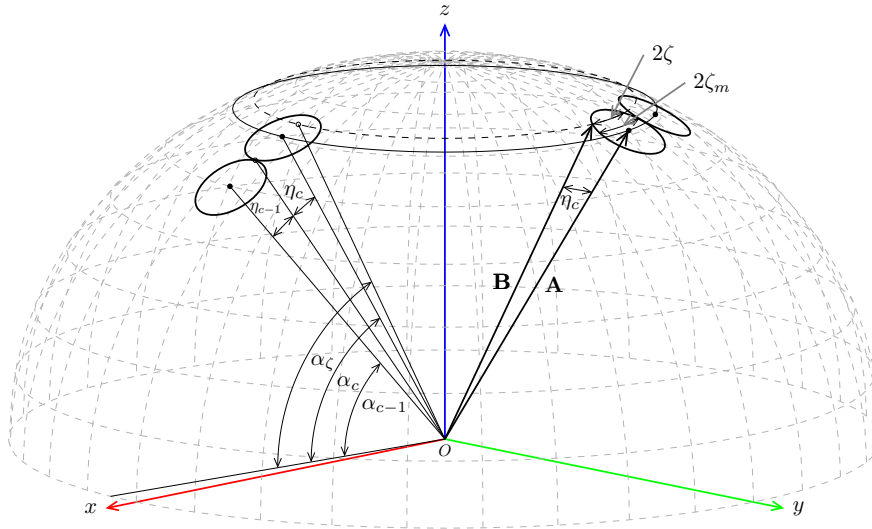


Figure 5.13: Diagram of vectors and angles defined in the problem.

of a circular cross-section parallel to the base plane and passing through the detector is denoted as 2ζ in Figure 5.13. Then α_c is the elevation angle of the respective circle. It

5. INITIAL POINT CONFIGURATIONS

is clear that the maximal arc angle ζ_m is determined by the number of detectors in the c -th ring:

$$\zeta_m = \frac{\pi}{n_c}. \quad (5.5)$$

Our goal is to determine the dependence of the angle ζ_m as a function of η_c . For this purpose we will describe vectors **A** and **B** from Figure 5.13 in spherical coordinates (R, α_c, γ_c) and $(R, \alpha_\zeta, \gamma_\zeta)$. The angle between these vectors is η_c . Their scalar product is:

$$R^2 \cos \eta_c = R^2 \cos \alpha_c \cos \gamma_c \cos \alpha_\zeta \cos \gamma_\zeta + R^2 \cos \alpha_c \sin \gamma_c \cos \alpha_\zeta \sin \gamma_\zeta + R^2 \sin \alpha_c \sin \alpha_\zeta. \quad (5.6)$$

We can assume that the azimuth of the vector **A** is $\gamma_c = 0$. Then $\gamma_\zeta = \zeta$ and the equation (5.6) is simplified:

$$\cos \zeta = \frac{\cos \eta_c - \sin \alpha_c \sin \alpha_\zeta}{\cos \alpha_c \cos \alpha_\zeta}. \quad (5.7)$$

Derivative of (5.7) with respect to α_ζ is:

$$\frac{d \cos \zeta}{d \alpha_\zeta} = \frac{\cos \eta_c \sin \alpha_\zeta - \sin \alpha_c}{\cos \alpha_c \cos^2 \alpha_\zeta}. \quad (5.8)$$

An extreme of (5.7) can be found from the condition $\frac{d \cos \zeta}{d \alpha_\zeta} = 0$ resulting in:

$$\sin \alpha_{\zeta_m} = \frac{\sin \alpha_c}{\cos \eta_c}, \quad (5.9)$$

where α_{ζ_m} is the elevation angle with the maximal arc length. Substituting this angle back into the equation (5.7) and simplifying it will bring the equation:

$$\cos \zeta_m = \frac{(\cos^2 \eta_c - \sin^2 \alpha_c)^{\frac{1}{2}}}{\cos \alpha_c}. \quad (5.10)$$

Substituting the term α_c from (5.4) and ζ_m from (5.5) into (5.10) we obtain the final non-linear equation:

$$\frac{[\cos^2 \eta_c - \sin^2 (\alpha_{c-1} + \eta_{c-1} + \eta_c)]^{\frac{1}{2}}}{\cos (\alpha_{c-1} + \eta_{c-1} + \eta_c)} = \cos \left(\frac{\pi}{n_c} \right). \quad (5.11)$$

This equation for η_c has to be solved numerically for certain n_c , knowing the α_{c-1} and η_{c-1} from previous calculations. In our case we have used the Dichotomy method [6]. For the first step to determine α_1 and η_1 we take the values $\alpha_{c-1} = \eta_{c-1} = 0$. If the viewing angle of the c -th ring is smaller than that of the ring $c - 1$, then the viewing angle of the ring $c - 1$ is iteratively decreased until the viewing angles of the two circles are equal.

The azimuth angle of each detector is not taken into account in this method, because detectors are lying on the top of each other. Since detectors of each ring are distributed equidistantly in the azimuth, the only parameter is the initial offset. In principle rotating the ring in the azimuth direction allows us to choose the position where the greater viewing angle is allowed.

6. RESULTS

The main goal of this work is to find an optimal configuration of circular detectors on a hemispherical surface. We have simplified this problem to the optimal configuration of N points on a surface of unit sphere to describe it mathematically better. The only variable of the simplified problem is the actual number of points N . The relation to our original problem can be expressed by expanding the unit sphere to our detection sphere radius $R = 160$ mm and demanding mutual distance of points on such a sphere to be $r = 3$ mm, which is the diameter of our detector.

In general the right way to determine the number of points is to choose N , then find an optimal solution and measure mutual distances. If the mutual distance is too small decrease N , if it is large then increase N and optimize the positions again. However, this approach is not useful. On one hand there is no proof that our solution is the optimal one and on the other hand finding the optimum is challenging task on its own.

We can rather measure the mutual distance of points in our initial configurations and then optimize them to achieve better results. In this chapter we will discuss features of initial point configurations and then we will try to choose the promising initial configurations which will be then optimized by the repulsion forces approach.

Since the number of points generated by polyhedral breakdown systems is not continuous (N is a function of frequency ν), let us start to study their features at the first place and then compare them to the spiral points approach and the parallel rings solution.

6.1. Polyhedral breakdown systems

To describe the system, we will use the s -energy and the mutual distance distribution of each configuration. We will take the distance of a point to its closest neighbour as a mutual distance of points. To describe the differences between methods and polyhedrons used better, we always take more frequencies to achieve wider overview of the breakdown system features.

The platonic solid with the lowest number of faces is the tetrahedron, the relation between number of points and the frequency of subdivision ν can be expressed using the equation:

$$N_{1,2} = 2\nu^2 + 2, \quad (6.1)$$

for methods 1 and 2. For methods 3 and 4 the equation is:

$$N_{3,4} = 1.5\nu^2 + 2. \quad (6.2)$$

The mutual distance in Figure 6.1 is the mean of mutual distances for each point. The colour shadow is the standard deviation of the mutual distances. Each point of the curve in Figure 6.1 corresponds to a certain frequency. There are two reasons for plotting the dependence on the number of generated points and not on the frequency. Firstly the relation of N as a function of ν changes with the method, especially when methods 3 and 4 are valid only for the even frequencies. Secondly the range of frequencies, which results in the mutual distance approximately equal to 3 mm, is also different for each method.

6.1. POLYHEDRAL BREAKDOWN SYSTEMS

To emphasize the variation of the distribution, we also determined the relative deviation as a ratio of the standard deviation and the mean value of the mutual distances. This is shown in Figure 6.2. The last parameter of the initial configuration is the s -energy. S -energies corresponding to frequencies and distances we have studied are depicted in Figure 6.3. To understand better the variations of mutual distances, Figure 6.4 shows histograms for each generated subdivision system of the tetrahedron. Bars on the mutual distance 0 determine the relative frequency of distance 3 mm. Colour of the bars is proportional to the number of generated points for frequency, which is denoted above the type of method.

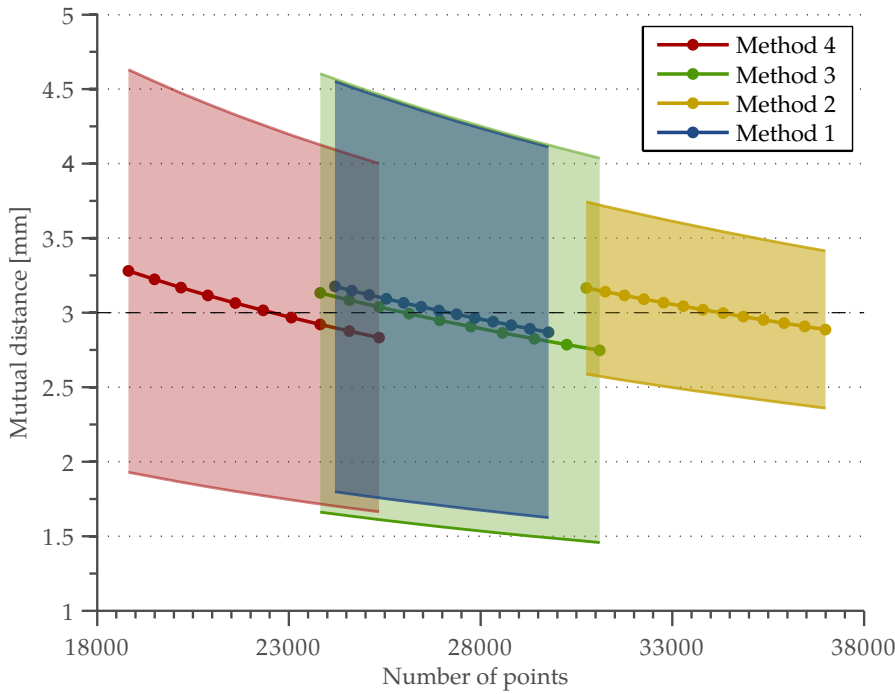


Figure 6.1: Dependence of the mutual distance on the number of points created by the subdivision of the tetrahedron. Colour shadows are standard deviations of the mutual distance distribution.

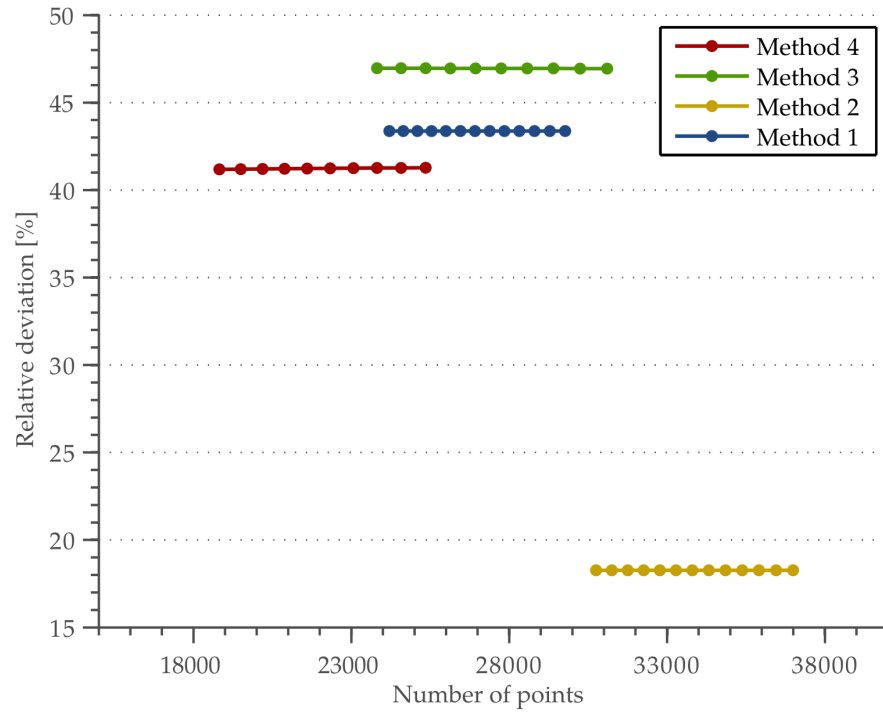


Figure 6.2: Relative deviation of the mutual distances created by the subdivision of the tetrahedron as a ratio of the standard deviation and the mean value.

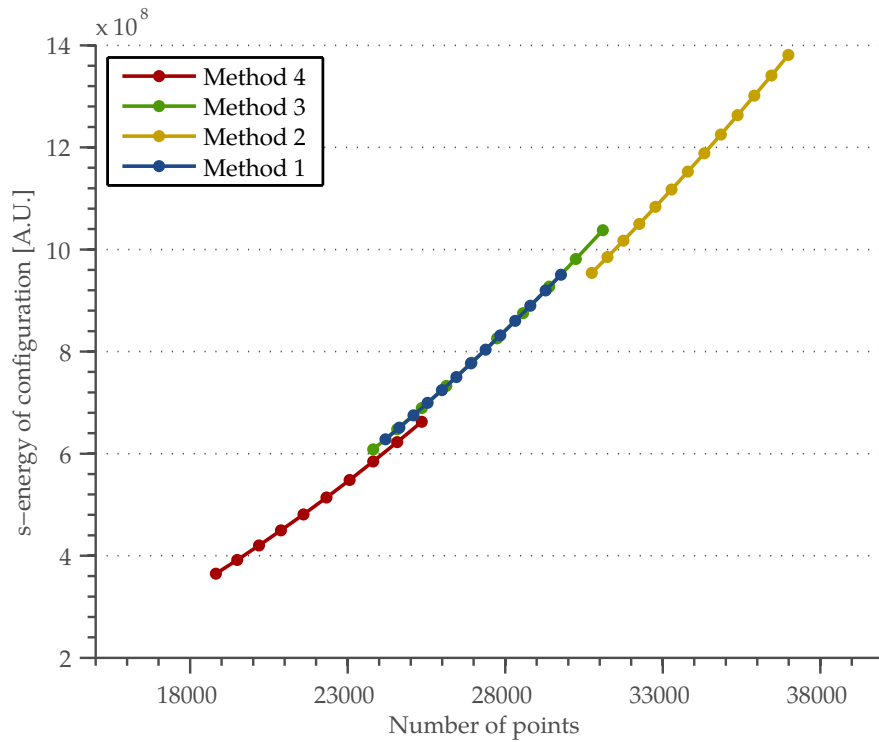


Figure 6.3: S -energy of initial configurations created by the subdivision of the tetrahedron for four basic methods.

6.1. POLYHEDRAL BREAKDOWN SYSTEMS

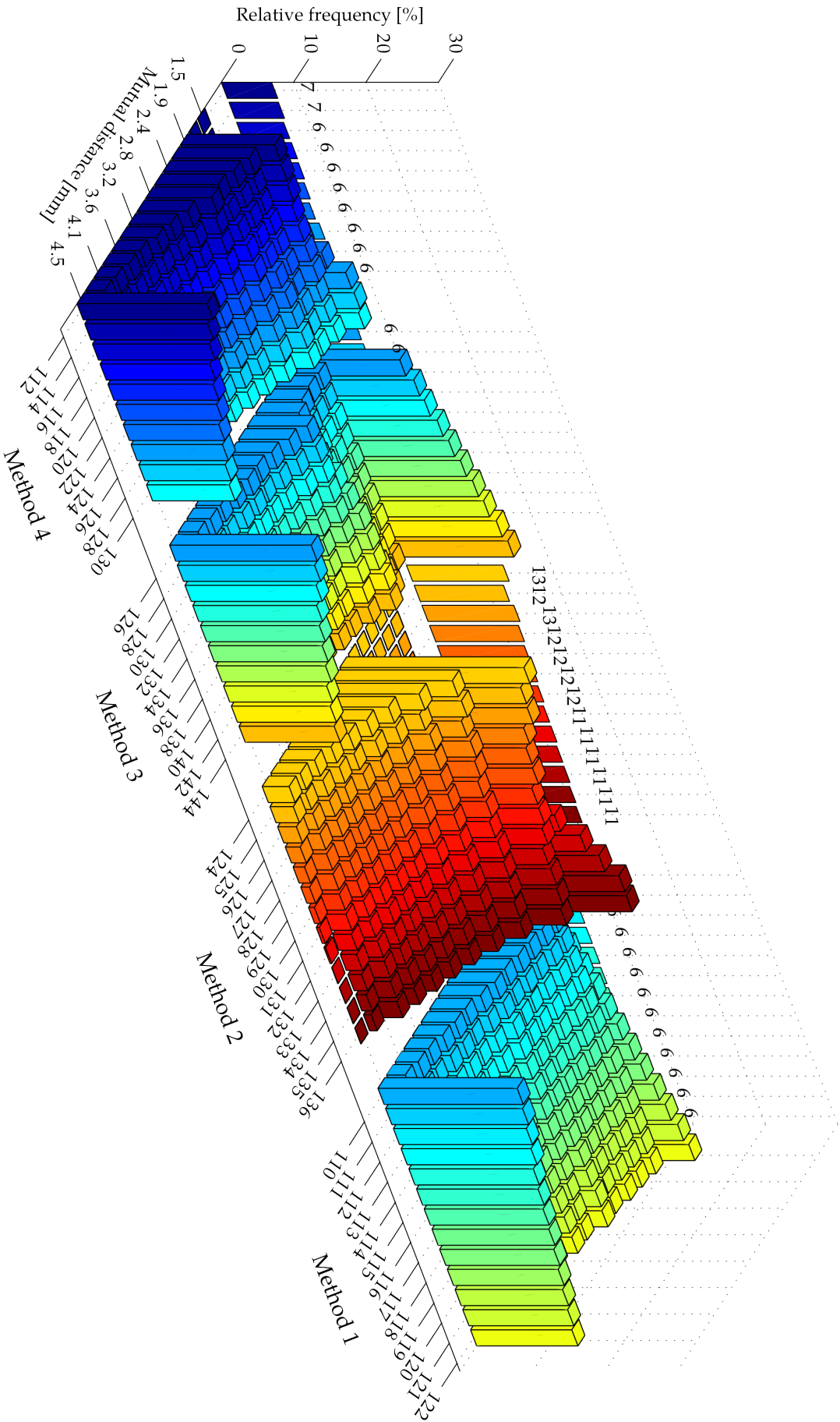


Figure 6.4: Histograms of the frequency of mutual distances for tetrahedron breakdown systems. Numbers above the method type are corresponding to frequencies. The colour is proportional to the number of points in the respective system. High peaks on the borders of the histogram are caused by the rest of distances which do not fit into the chosen classes.

As it was written in Chapter 5, tetrahedron breakdown systems suffer from the high variation of mutual distances. This is caused by high frequencies which are needed for generating the high count of points. Regarding the differences between methods of subdivision, method 2 seems to have superior properties that are the lowest mutual distance variability and also the lowest s -energy for the given number of points.

The second polyhedral breakdown system is the octahedron system. The equation determining the number of points as a function of frequency ν is as follows:

$$N_{1,2} = 4\nu^2 + 2, \quad (6.3)$$

for methods 1 and 2. For methods 3 and 4:

$$N_{3,4} = 3\nu^2 + 2. \quad (6.4)$$

The mean of mutual distances is shown in Figure 6.5. There are only two groups of frequencies, mainly because of the fact that methods 3 and 4 require even frequencies. In this case the range of frequencies for methods 1 and 2 is $\nu_{1,2} = \langle 88, 100 \rangle$, then for methods 3 and 4 $\nu_{3,4} = \langle 100, 118 \rangle$. You can see that curves corresponding to methods 1 and 2 are almost the same, but method 2 shows significantly lower mutual distance variation. This is depicted in Figure 6.6 where the relative deviation as a function of the number of points generated is plotted. The s -energy of the generated system is independent on the method used, there is only small improvement for method 2 (see Figure 6.7). In this case the histograms of relative frequencies are far more important, as you can see in Figure 6.8. Method 2 mutual distances distribution fits much better into the range of classes compared to other methods where some frequencies show the significant number of distances laying on the border of the histogram range.

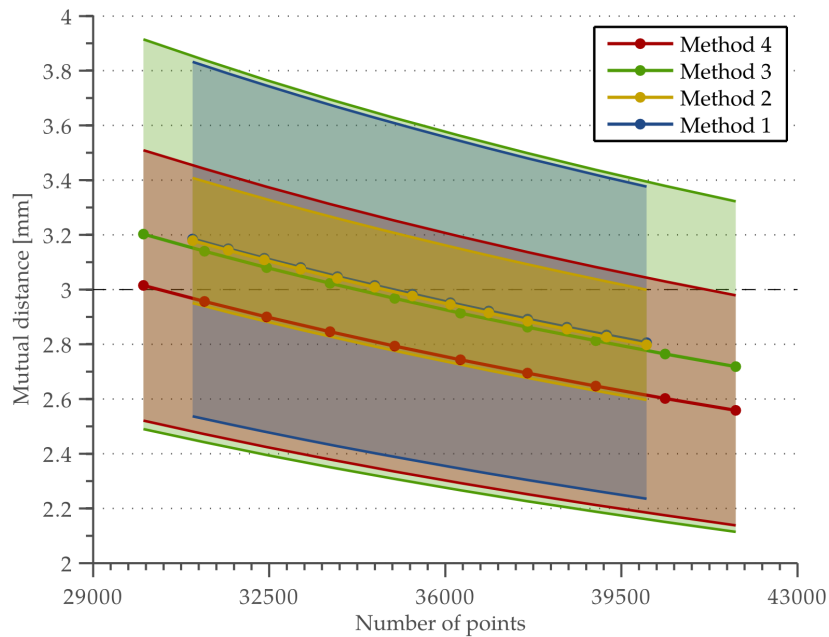


Figure 6.5: Octahedron breakdown systems mutual distance as a function of the number of points generated. The shadow determines the standard deviation of mutual distances.

6.1. POLYHEDRAL BREAKDOWN SYSTEMS

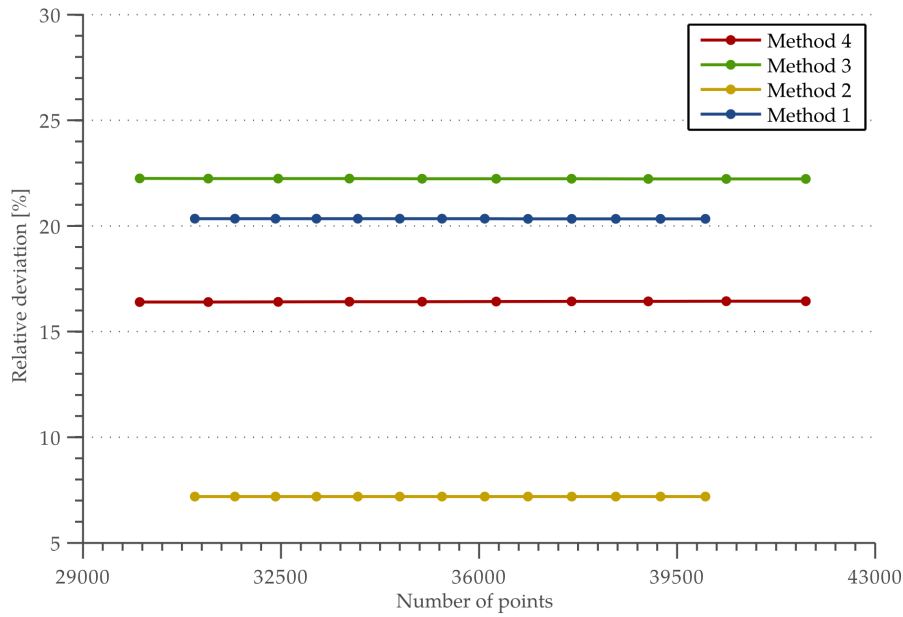


Figure 6.6: Octahedron breakdown system mutual distances relative deviation as a function of the number of points generated.

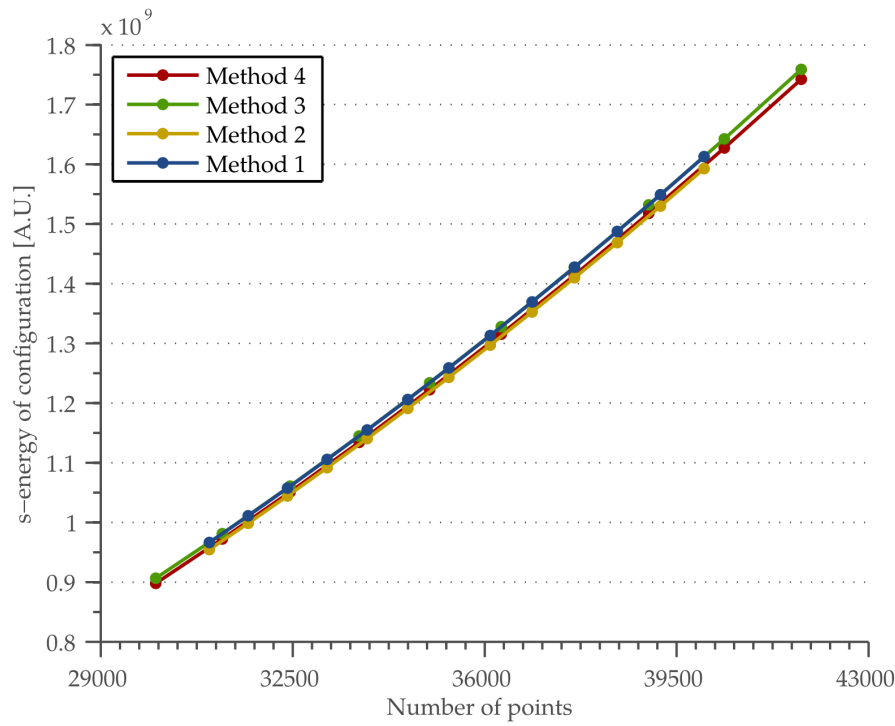


Figure 6.7: Octahedron breakdown system s -energy differences for four methods of subdivision on different frequencies.

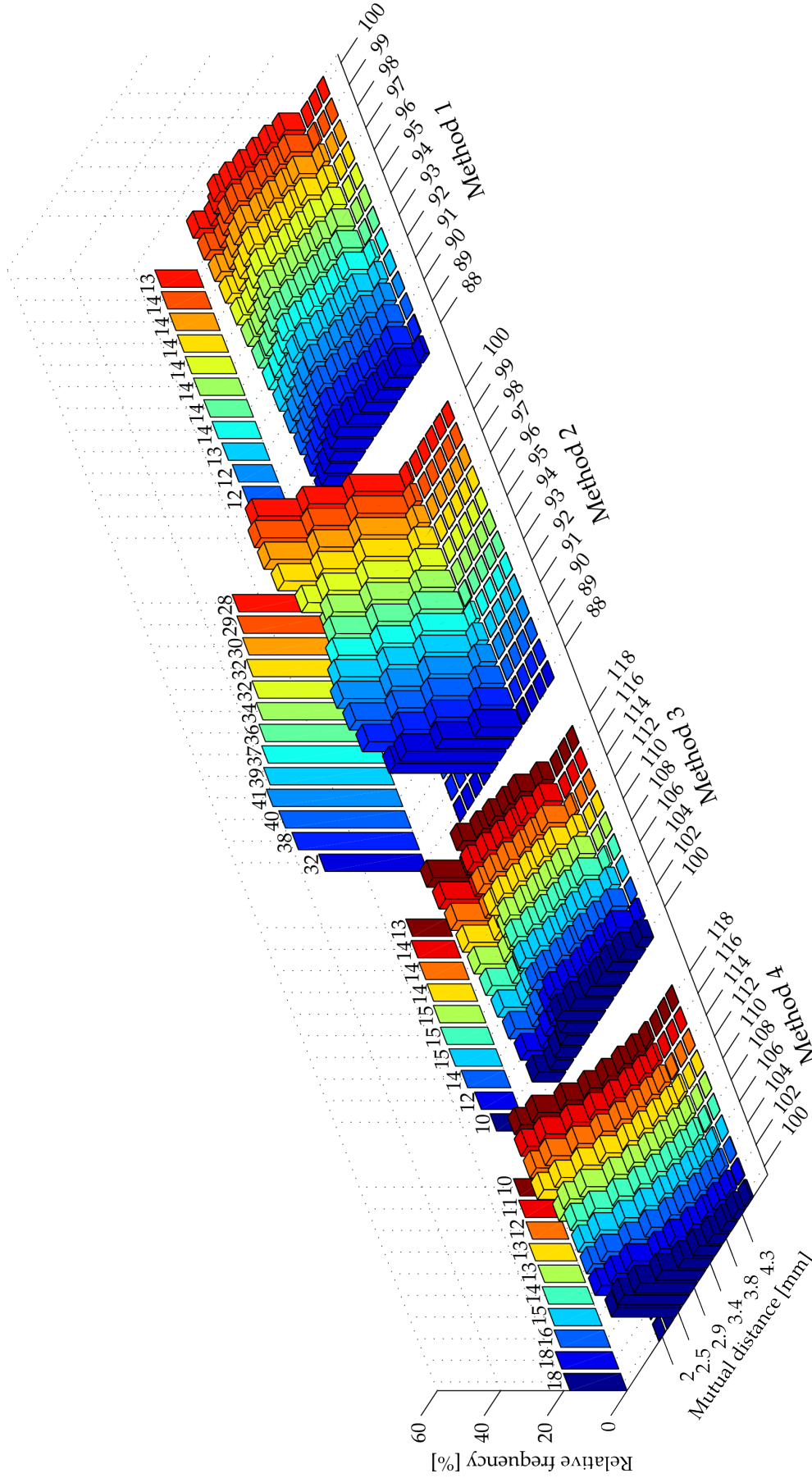


Figure 6.8: Histogram of the relative frequency of mutual distances for octahedron breakdown systems. Numbers above the method type are corresponding to frequencies. The colour is proportional to the number of points in the respective system. The high peaks on the borders of the histogram are caused by the rest of distances which do not fit into the chosen classes.

6.1. POLYHEDRAL BREAKDOWN SYSTEMS

The last polyhedron of our interest is the icosahedron. The number of points generated by subdivision methods 1 and 2 for frequency ν is:

$$N_{1,2} = 10\nu^2 + 2. \quad (6.5)$$

For methods 3 and 4 is the relation as follows:

$$N_{3,4} = 7.5\nu^2 + 2. \quad (6.6)$$

The possibility of employing lower frequency results in the smaller variation of mutual distances. This can be seen in dependence of the mean mutual distance (see Figure 6.9) and the relative mutual distance deviation (Figure 6.10). The difference in the s -energy for systems generated with various methods shown in Figure 6.11 is undistinguishable. From histograms in Figure 6.12 it is clear that method 2 applied to the icosahedron subdivision has the significant advantage over the other methods and polyhedrons regarding the uniformity of mutual distances.

Next section is devoted to the spiral points. We try to create approximately the same number of the points and compare their uniformity with the points achieved by breakdown systems. The breakdown systems chosen to be compared are systems which had maximal relative frequency in the class with centre 3 mm.

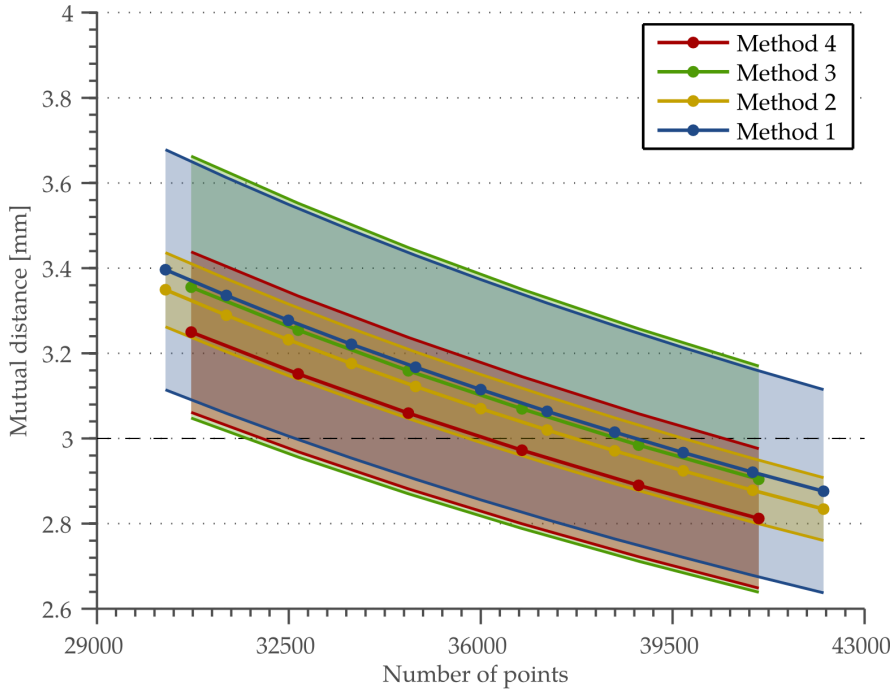


Figure 6.9: Mutual distance dependence on the number of points generated by icosahedron breakdown systems. The shadow determines the standard deviation of mutual distances.

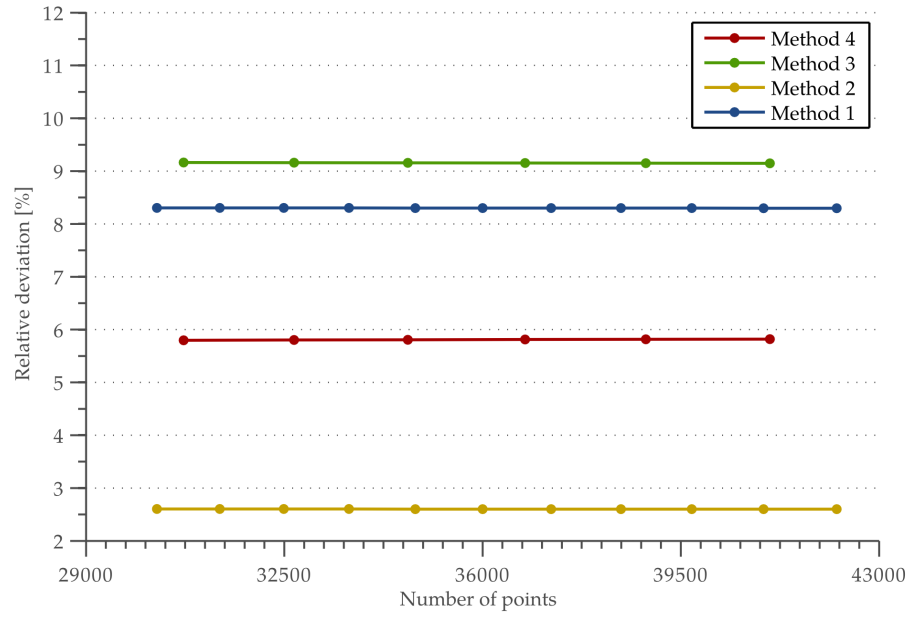
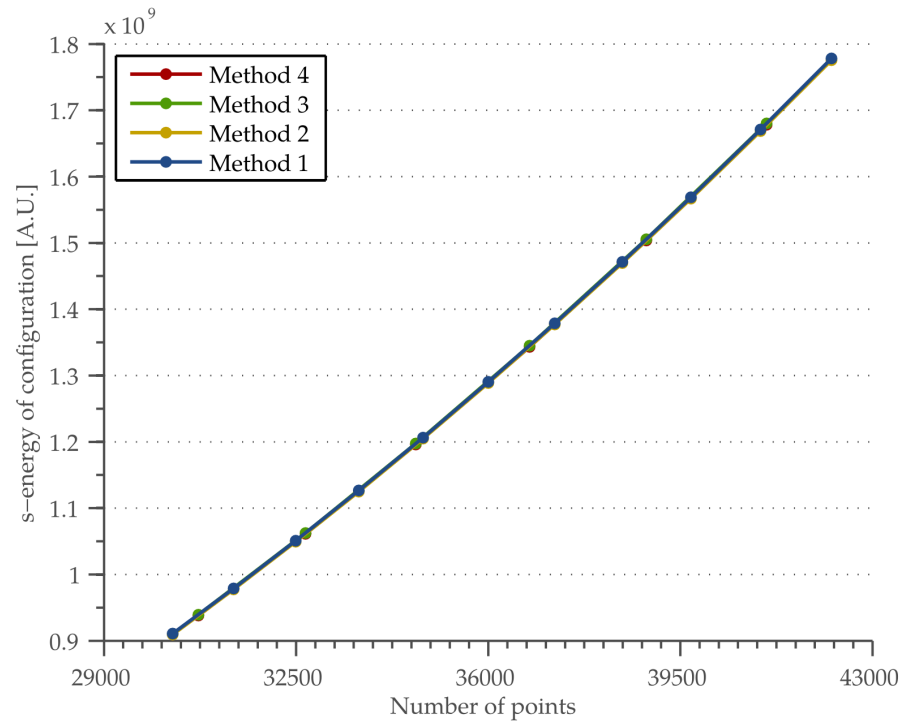


Figure 6.10: Relative deviation of the icosahedron breakdown systems.

Figure 6.11: Icosahedron breakdown systems s -energy.

6.1. POLYHEDRAL BREAKDOWN SYSTEMS

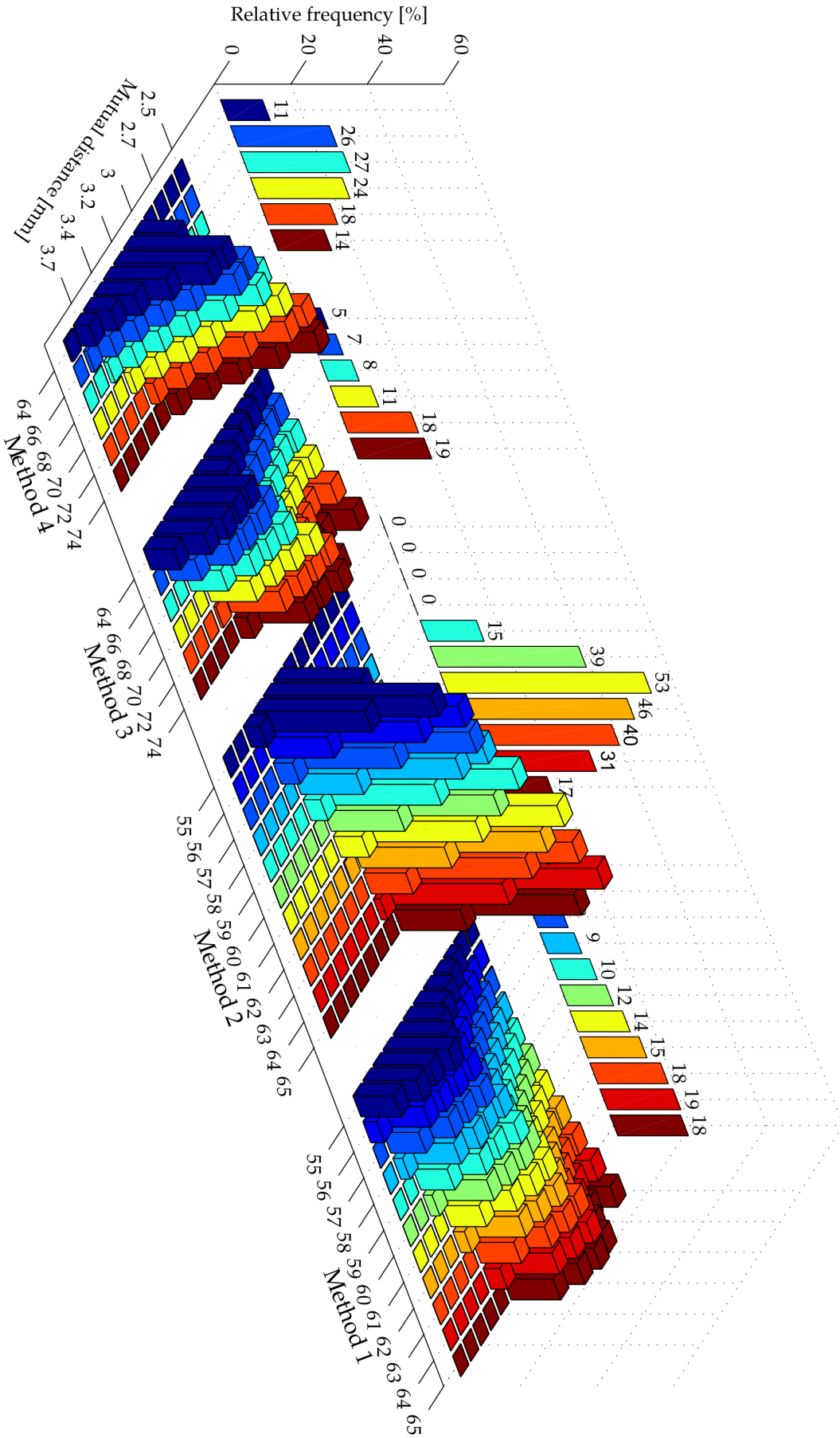


Figure 6.12: Histograms of the relative frequency of mutual distances for icosahedron breakdown systems. Numbers above the method type are corresponding frequencies. The colour is proportional to the number of points in the respective system.

6.2. Spiral points

As it was written in the beginning of this chapter, the only variable for the optimal solution of our problem is the total number of detectors N . But different initial configuration approaches requires additional constants to be involved. In the previous section we dealt with polyhedral breakdown systems for which the frequency of subdivision ν and the chosen method of PPT subdivision play the major role. There is only one term that can be varied apart from the total number of points in spiral systems. It is the azimuth distance factor $\frac{3.6}{\sqrt{N}}$. To have comparable results as a desired number of points we will choose two most optimal distributions of the octahedron and the icosahedron breakdown systems and then the average value of these four. Used numbers are presented in Table 6.1:

Type of polyhedron	Subdivision method	Subdivision frequency	Number of points
Icosahedron	2	61	37212
Icosahedron	2	62	38442
Octahedron	2	90	32402
Octahedron	2	91	33126
Average of the above			35296

Table 6.1: Chosen numbers of points for spiral systems.

We varied the constant 3.6 in range from 3.0 to 4.0 and we made same statistic like in the previous section. The dependence of the mean mutual distance on the azimuth distance factor is shown in Figure 6.13. Shadows determine the standard deviation of mutual distances. The relative deviation in Figure 6.14 shows that it is merely constant with break around 3.55. This value is then chosen as an optimal azimuth distance factor.

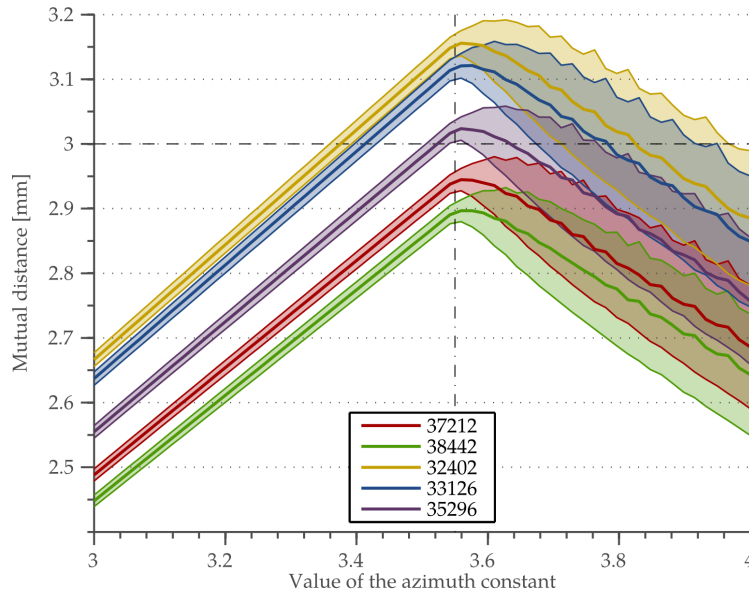


Figure 6.13: Mutual distance of spiral points as a function of the value of the azimuth distance factor. Curves correspond to numbers of points from Table 6.1.

6.3. PARALLEL RINGS

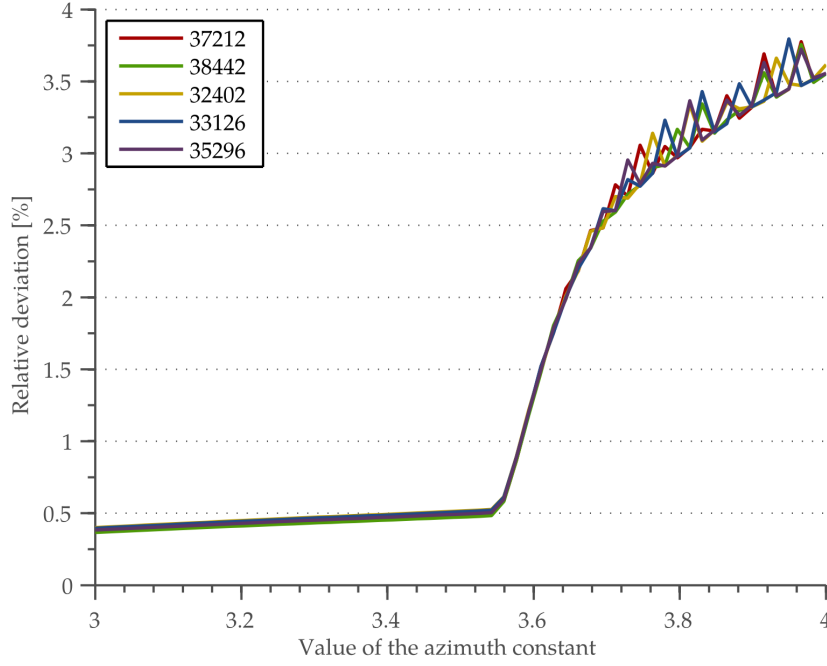


Figure 6.14: Relative deviation of spiral point's mutual distances as a function of the value of the azimuth distance factor. Curves correspond to numbers of points in Table 6.1.

6.3. Parallel rings

The last approach discussed in Chapter 5 is the parallel rings system of points. Compared to the previous two systems, this one needs quite a lot of preparatory work. We have to determine the number of rings C and the number of detectors in each ring n_c . This was done by a simple calculation of stacking the circles with the diameter 3 mm on a hemisphere with the radius 160 mm. Resulting numbers are in Table 6.2.

The total number of points is 17830, but this is valid only for a hemispherical distribution. To achieve comparable results we should mirror the points to simulate spherical configuration. This results into 35329 points. This is close to the average number of points from Table 6.1. We can vary the total number of points by adding some points to circles with the high count of points. On the other hand we may want to vary the number of points in the last ring to achieve better coverage on the pole. The denser sphere packing, which results in a smaller detector viewing angle, can be relaxed by rotating in the azimuth angle. This allows detectors to groove into spaces made in the previous ring. We do not want to vary the circle numbers because there is no clear method of doing it with preserving or achieving features of the distribution. For practical reasons we raised the number of points in the last ring to 3, to avoid placing the detector directly on the pole, where the light source is screened out by the detector itself.

c	n_c	c	n_c	c	n_c	c	n_c
1	335	22	308	43	234	64	124
2	334	23	305	44	229	65	118
3	334	24	303	45	225	66	112
4	334	25	300	46	220	67	106
5	333	26	297	47	215	68	100
6	333	27	294	48	210	69	94
7	332	28	291	49	205	70	88
8	331	29	288	50	200	71	82
9	330	30	285	51	195	72	76
10	329	31	281	52	190	73	70
11	328	32	278	53	185	74	64
12	327	33	274	54	180	75	58
13	325	34	271	55	174	76	51
14	324	35	267	56	169	77	45
15	322	36	263	57	164	78	39
16	321	37	259	58	158	79	33
17	319	38	255	59	152	80	26
18	317	39	251	60	147	81	20
19	315	40	247	61	141	82	14
20	312	41	243	62	135	83	8
21	310	42	238	63	130	84	1

Table 6.2: Calculated number of the detectors n_c for the c -th ring.

6.4. Repulsion forces

In this section we submit all twelve initial configurations to the repulsion forces optimizing algorithm. To achieve comparable data of the optimization process, we performed 1000 iterations of optimization for each initial configuration. The amount of the time that the calculation took is presented in Table 8.1. Figure 6.15 shows the development of the mean mutual distance over the optimization process. Equivalent numbers of points for different methods has the same colour. One can see that the mean of the mutual distances in case of the icosahedron breakdown systems is decreasing and the mean of the mutual distances for the same number of spiral points is increasing. We can say that equivalent numbers of points approach the same value.

6.4. REPULSION FORCES

Type of the method	Number of points	Time consumed [s]
Icosahedron breakdown, $\nu = 61$	37212	2985
Icosahedron breakdown, $\nu = 62$	38442	3213
Octahedron breakdown, $\nu = 90$	32402	3009
Octahedron breakdown, $\nu = 91$	33126	2379
Spiral points of icosahedron $\nu = 61$	37212	2997
Spiral points of icosahedron $\nu = 62$	38442	3215
Spiral points of octahedron $\nu = 90$	32402	3027
Spiral points of octahedron $\nu = 91$	33126	2377
Average number of points	35296	2706
Parallel rings	35329	2709

Table 6.3: Initial configurations, which were optimized, and the time needed to perform 1000 iterations of the optimizing algorithm.

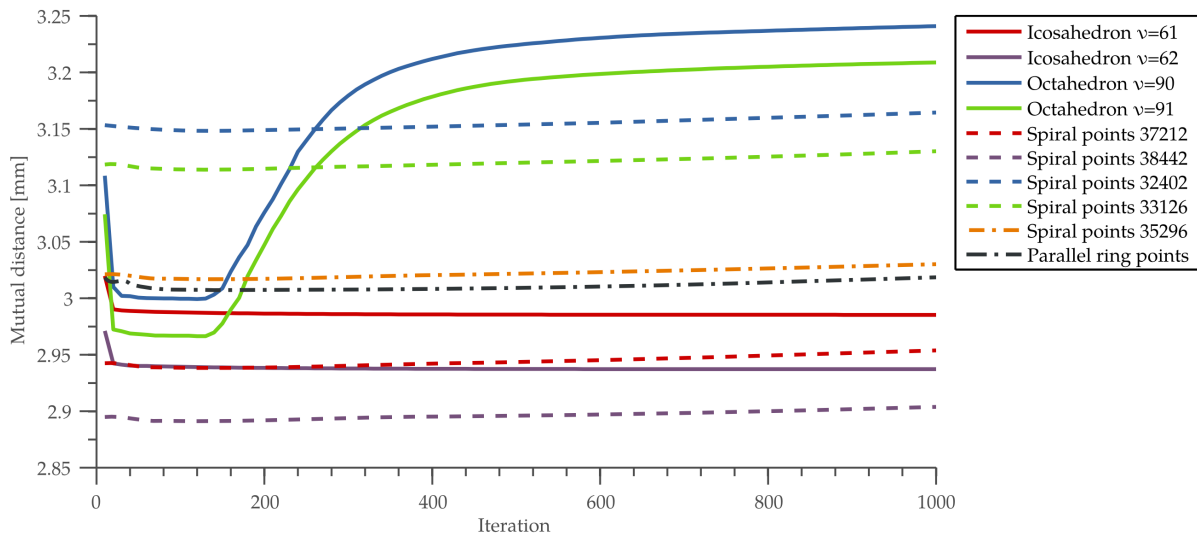


Figure 6.15: Mean value of the mutual distances progress during the optimization process.

The relative deviation is rapidly changing only in the beginning of the simulation as it is depicted in Figure 6.16. For icosahedron breakdown systems is the relative deviation preserved. The spiral points method and the parallel rings method are approaching this value. On the other hand the octahedron breakdown system starts with higher relative deviation which then decreases and stays constant, but higher than other methods.

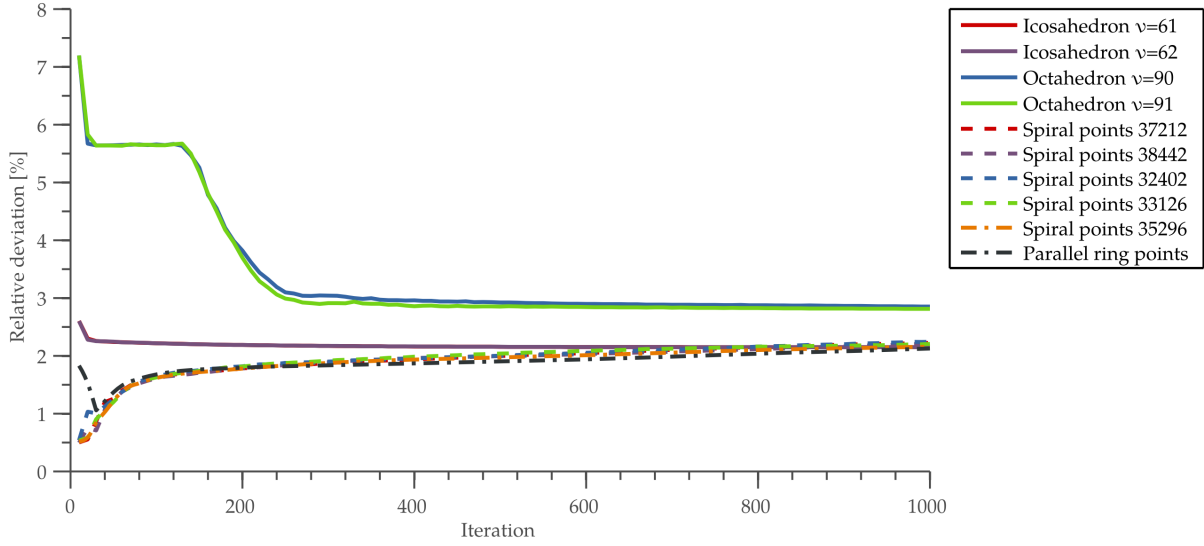


Figure 6.16: Relative deviation of the mutual distances development over the optimization procedure.

The word optimized in this case means that the s -energy of the configuration was lowered. Mathematically it is a better configuration regarding the minimal distance of points. When describing the results we took as the mutual distance of i -th point the distance to the closest neighbour. As the mutual distance of the configuration the mean value of these particular mutual distances was taken. This approach can be misleading in the case of scattered pairs of points, where the distance to the closest neighbour is always the same, but the uniformity of the whole configuration is lost. This is the case of spiral points, where we place the points next to each other purposely, for this reason the relative deviation of mutual distances is raising in Figure 6.16.

To choose the optimal configuration as a result of this thesis an experiment should be performed. The application of results from this chapter on the problem of measurements done by means of SM II is described in the next chapter.

7. APPLICATIONS

In the previous chapter we ended with ten initial configurations of points which were then optimized. To measure in these new sets of positions, we should perform some post-processing of the results. The main reason is the angular resolution of SM II and also the fact that we only measure the hemispherical distribution of the light intensity scattered from the sample surface. The non-overlapping is mathematically assured by defining the detector diameter as the smallest distance of two points in the set. This is not possible in our problem where we have the detector with the fixed diameter. As the first step of the post-processing we want to discriminate configurations with mutual distances different from our detector dimensions. The second step of the data post-processing is creating a sequence of measurement points from a given initial configuration of points in the form, which will be directly executable by SM II.

7.1. Visualizing spherical points

To discriminate the configurations according to variability in mutual distance, its mean value and standard deviation are not enough. To analyse the initial configuration we wanted to visualize the detector positions. The process of visualization and resulting images are described in this section.

We are mapping each point of the initial configuration to a circle with the diameter 3 mm on a spherical surface with the radius 160 mm. The centre of the circle is identical with the respective point. Because creating the circle with the given centre and the diameter as an intersection of a plane and a unit sphere is complicated, we took a shortcut. We have started with a spherical cap with the desired diameter situated on the pole. Then we have applied two rotational matrices on the vertices of a spherical cap to rotate it around the x and then around the z axis. The position vector of a single spherical cap point $[x_i, y_i, z_i]$ linked to the i -th point of the given configuration can be expressed by the equation:

$$\begin{bmatrix} x_i \\ y_i \\ z_i \end{bmatrix} = \begin{bmatrix} \cos \phi_i & -\sin \phi_i & 0 \\ \sin \phi_i & \cos \phi_i & 0 \\ 0 & 0 & 1 \end{bmatrix} \cdot \begin{bmatrix} 1 & 0 & 0 \\ 0 & \cos \theta_i & -\sin \theta_i \\ 0 & \sin \theta_i & \cos \theta_i \end{bmatrix} \cdot [x_0 \ y_0 \ z_0], \quad (7.1)$$

where $[x_0, y_0, z_0]$ is the position vector of a corresponding point of the spherical cap on the pole, θ_i is the declination angle of the given point of a spherical configuration and ϕ_i is the azimuth angle of the given point of the spherical configuration. We have applied the visualization routine on an original configuration of points, which were equidistantly distributed around the azimuth rotational axis and the declination axis, the resulting visualization is depicted in Figure 7.1. Details on the top of the figure shows that close to the equator the detectors are touching each other (top left) and with a smaller declination angle the detectors are more and more overlapping (top right).

According to the results of Chapter 6 we have chosen only three initial points configurations, one for each approach. As an exemplar of the breakdown systems we took the icosahedron frequency 61 system. The best spiral points system is the spiral system of 35296 points. There is only one configuration that we tested for the case of parallel rings. We have improved the visualization by colouring the circles with the colour

7.1. VISUALIZING SPHERICAL POINTS

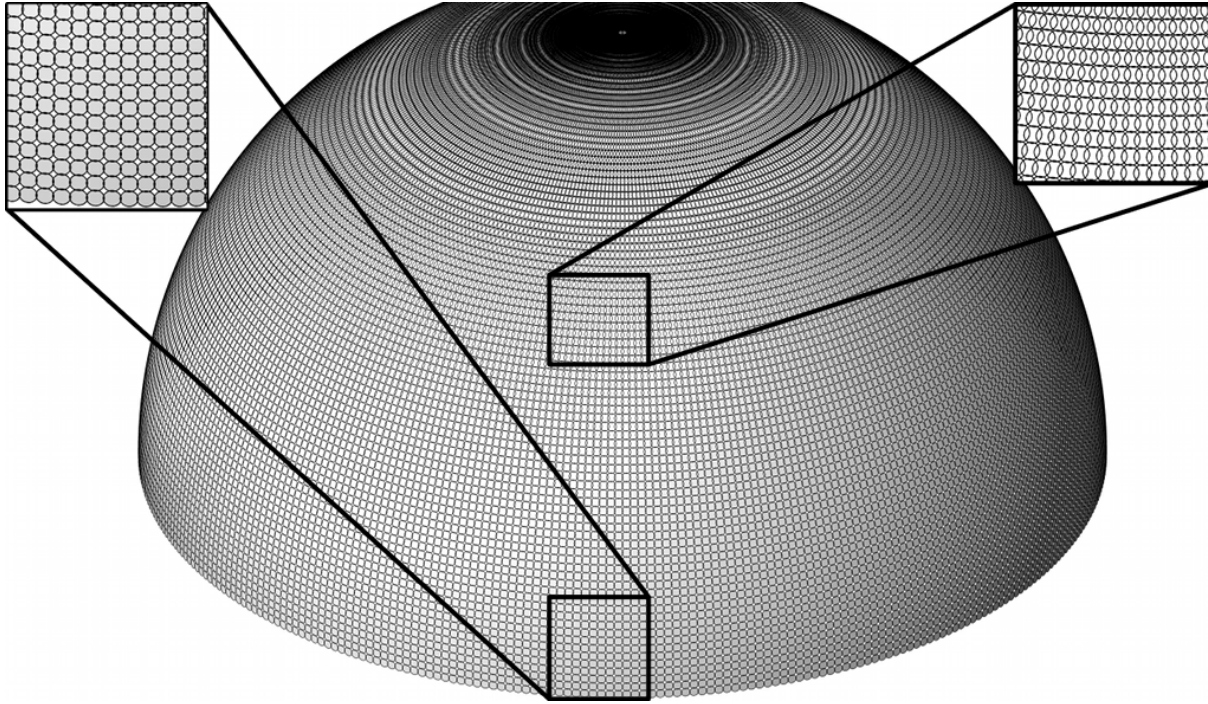


Figure 7.1: Visualization of the old measurement's points configuration. The detail on the top left shows non-overlapping detectors placed near the equator. The top right detail shows overlapping of the detectors with decreasing declination angle.

representing the difference between its closest neighbour and the diameter of detector (3 mm).

The icosahedron frequency 61 breakdown system initial configuration created by method 2 is shown in Figure 7.2 (left). The optimized system preserves symmetry and shows lower variation in the mutual distances (Figure 7.2, right).

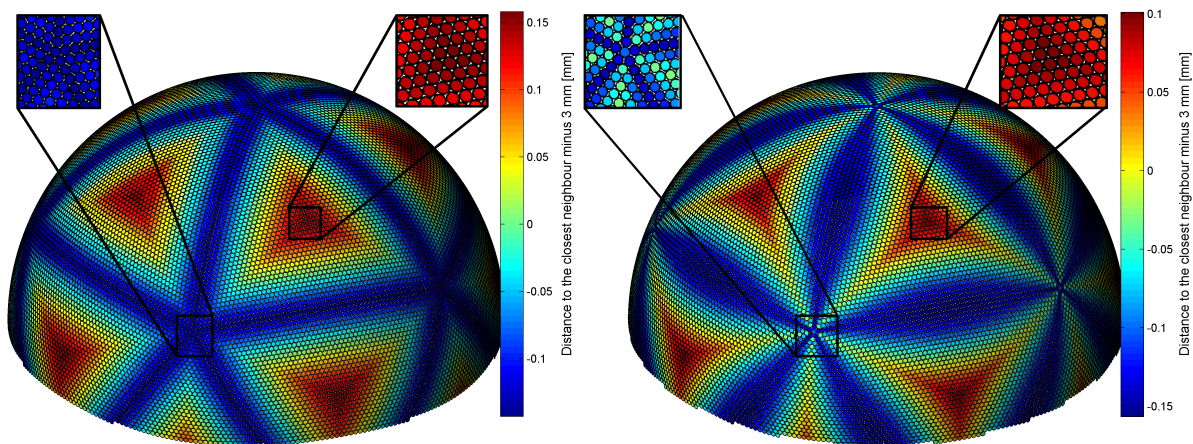


Figure 7.2: Icosahedron frequency 61 breakdown system created by method 2, with detailed view of dense and loose locations is the left. On the right side is the same system, but after 1000 steps of optimization. Detailed locations are approximately the same in both systems. The colour is defined as the difference of the distance to the closest neighbouring point and the real detector diameter 3 mm.

The analysis of the spiral point system's visualization is more complicated. As we have previously mentioned the statistics of the closest neighbour can be misleading for the case of the spiral points systems. This is shown in Figure 7.3, where on the left side the initial configuration seems to be uniform except for the zoomed area on the pole of the hemisphere, where the defects are enormous. To reduce the effect of the pole on the whole visualization the colour bar range is modified. Respective values in the zoomed part are in the range from -1.15 to 0.1 mm. Optimization of such an initial configuration is shown in the right part of Figure 7.3. The uniformity is broken, but according to the colour bar range the variation is lower, ranging roughly 10 % from the ideal distance of 3 mm.

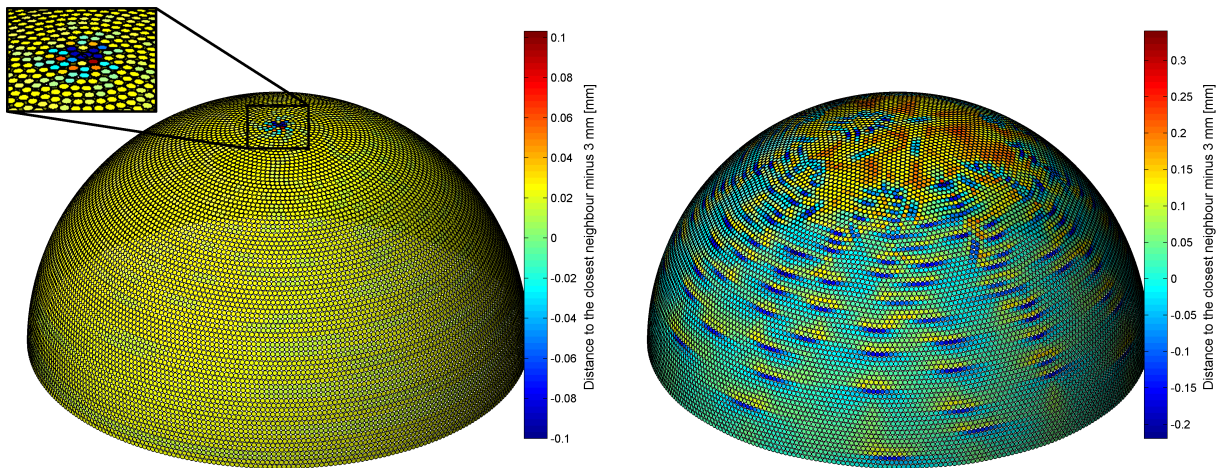


Figure 7.3: Spiral system of 35296 points initial configuration is visualized in the left part of picture. The detailed part on the pole is the main defect of the system. Because of this feature the colour scale was modified. The respective differences in the detailed area were in range from -1.5 to 0.1 mm. The optimized configuration on the right side shows better uniformity on the pole. Also the variation of the distances is lower. Unfortunately there seems to be no interesting details to be emphasized on the optimized configuration.

Figure 7.4 shows the parallel ring system initial configuration (left) and its optimization (right). Parallel ring systems are analogous to the spiral systems. The major difference is basically in the discrete declination angles in which detectors are intentionally situated in the parallel ring system. The analogy is observable in the right parts of respective visualizations (see Figures 7.3 and 7.4) where the depicted configurations after optimizing are not easily distinguishable. On the other hand the problem with the points on the pole is better solved in the case of parallel rings. This is shown on the top left part of Figure 7.4, the colour bar scale was not modified and the range of distances is smaller compared to the spiral points in Figure 7.3.

7.2. Generating the measurement sequence

The second step of the data post-processing is transforming the configuration of points on a hemispherical surface into the sequence of points measured by SM II. There is no order of points in the initial configuration especially for the case of breakdown systems

7.2. GENERATING THE MEASUREMENT SEQUENCE

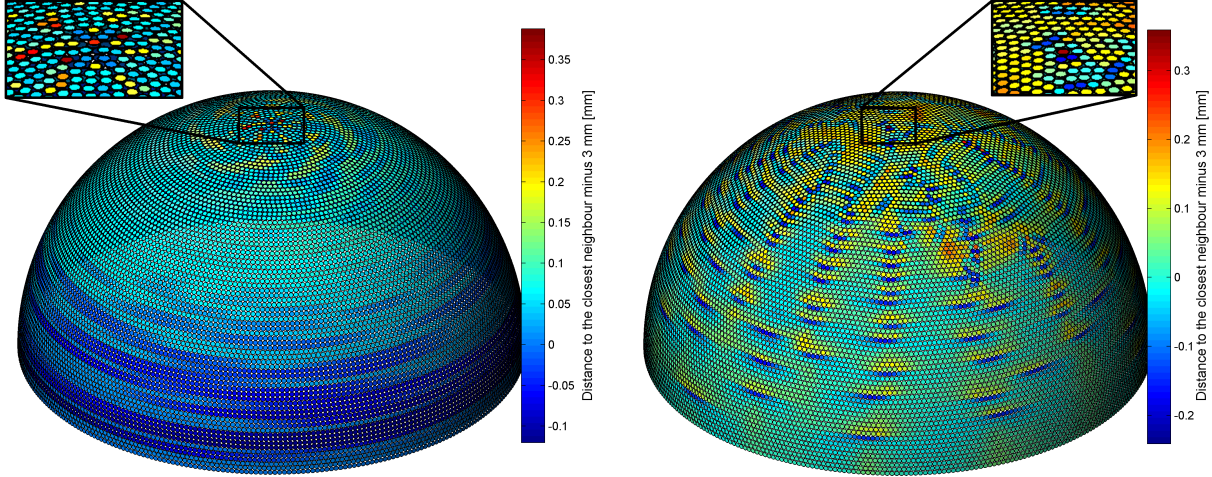


Figure 7.4: Visualization of the parallel ring system initial configuration (left), the detail in the top left corner shows the defects on the pole of the hemisphere. The distances on the pole of the initial configuration are more uniformly distributed than in the case of the spiral system initial configuration. The optimized configuration (right) is analogous to the one created from the spiral system initial points configuration shown on the right side of Figure 7.3.

where the points are created face by face. The default order of parallel rings or spiral point systems can be assumed as optimal, but it is not useful for SM II which is not capable of 360° rotation around the azimuth axis. The first step of obtaining the measurement sequence is transforming the points from the Cartesian coordinate system to our modified (hemi) spherical coordinate system. This is done using equations for spherical coordinates:

$$\phi_0 = \arctan \frac{y}{x} \text{ and} \quad (7.2)$$

$$\theta_0 = \arccos z. \quad (7.3)$$

After the calculation of spherical coordinates we need to translate these coordinates to our modified ones:

$$\phi = \begin{cases} \phi_0 & \text{if } \phi_0 < 180^\circ \\ \phi_0 - 180^\circ & \text{if } \phi_0 \geq 180^\circ \end{cases} \quad (7.4)$$

$$\theta = \begin{cases} -\theta_0 & \text{if } \phi_0 < 180^\circ \\ \theta_0 & \text{if } \phi_0 \geq 180^\circ \end{cases} \quad (7.5)$$

Then we treat the resulting azimuth coordinate ϕ and the declination coordinate θ as independent. We divide the azimuth coordinate angular range into intervals with a constant width, for example $(0^\circ, 0.5^\circ)$ for the width 0.5° . After that we sort all the points belonging to the chosen interval according to the angle of declination. To achieve a better performance we switch between the ascending and descending order in successive azimuth coordinate intervals. Then the detector measures on both the way forwards and also the way backwards. As an example we have generated the path with the azimuth coordinate interval width 10° for the icosahedron breakdown frequency 61 system optimized initial configuration (see Figure 7.5).

This method of generating measurement sequence depends only on the width of the azimuth coordinate intervals. This value determines the ratio between the amount

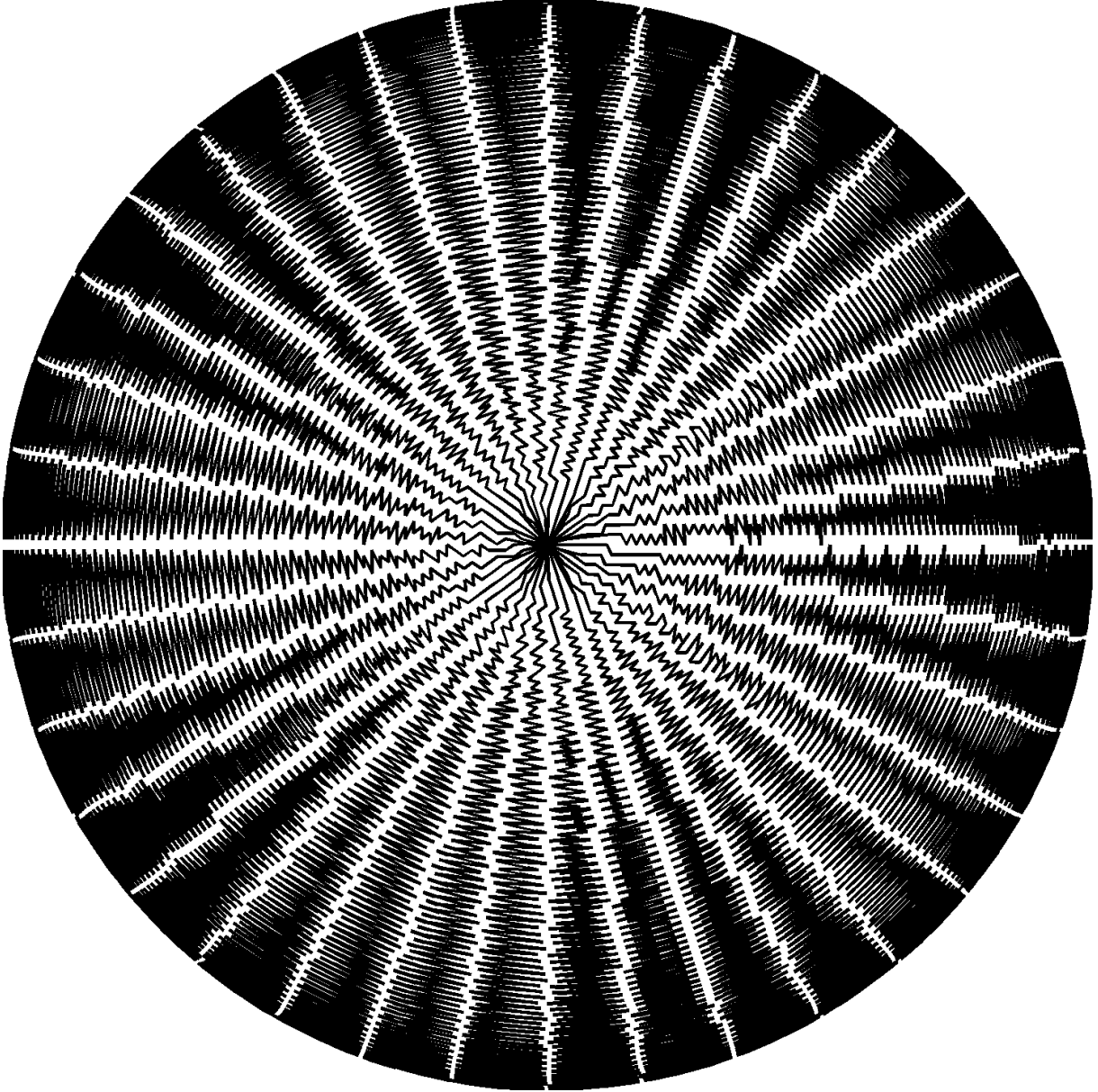


Figure 7.5: Detector trajectory visualization (solid black line) of the measurement sequence with the azimuth coordinate interval width 10° created for the icosahedron breakdown frequency 61 system optimized initial configuration.

of rotation performed around the azimuth and the declination axis as it is shown in Figure 7.6. The total time of measurement is then proportional to the length of the detector trajectory. In the comparison with the old measurement method used, one problem arises. The old method measures in a higher number of positions than it is necessary and optimal, but the length of the trajectory is very close to the minimal trajectory needed for travelling over the hemispherical surface.

To avoid moving of the detector to distant points we slightly improved the algorithm. Considering that there are fewer points around the pole of the hemisphere, one can presume that within each interval of the azimuth coordinate there will be long trajectories without measuring during the detector movement to the opposite side of the hemisphere. To exclude moving the detector through the pole we have divided the

7.2. GENERATING THE MEASUREMENT SEQUENCE

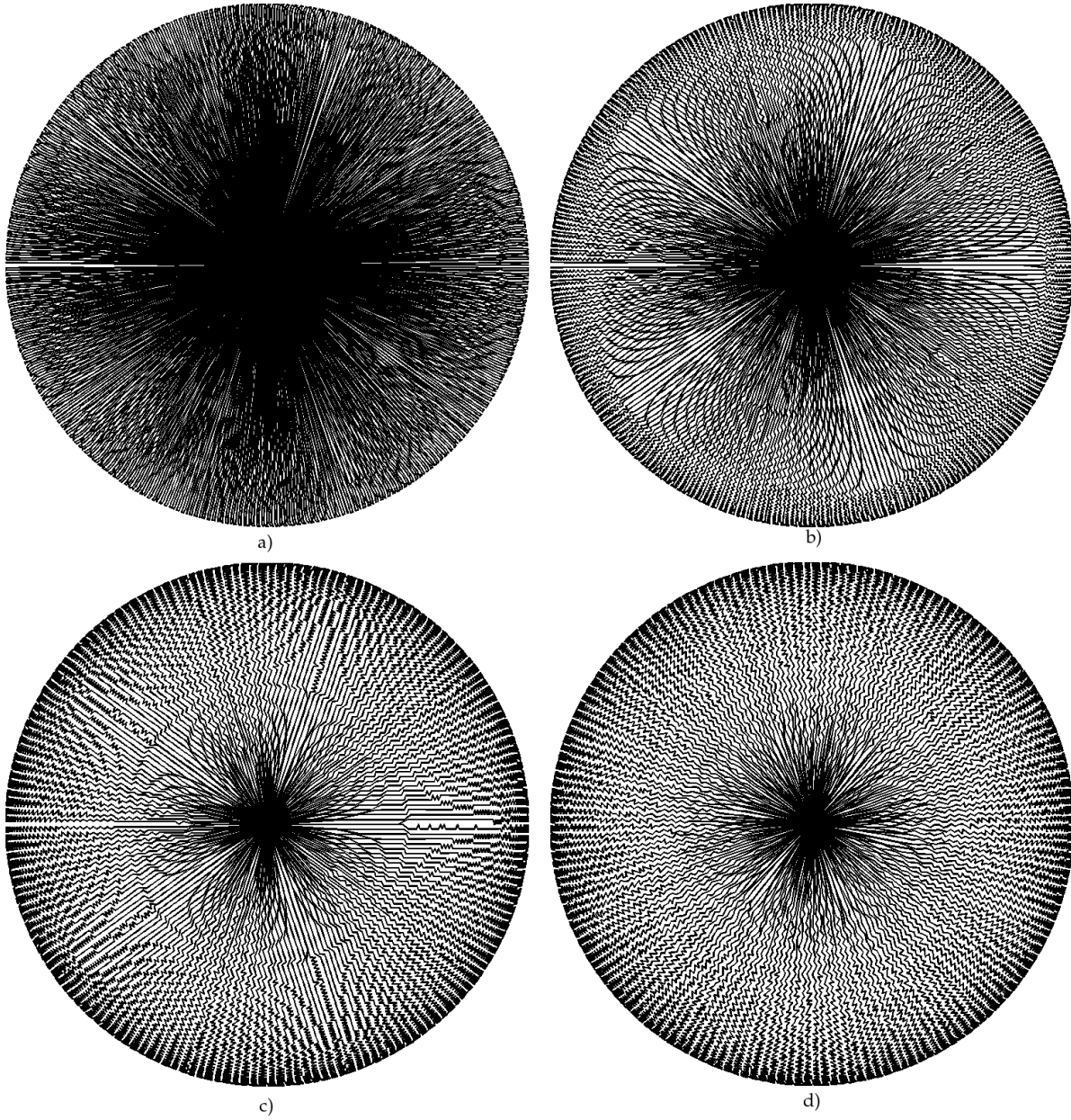


Figure 7.6: Four different measurement sequences. Sequences a),b) and c) are for different widths of azimuth coordinate intervals 0.5° , 1.0° and 2.0° for the respective cases created for the optimized icosahedron breakdown frequency 61 initial system and d) shows the sequence with the azimuth coordinate interval width 2° for the optimized 35296 spiral system initial configuration.

configuration of points into two groups. One group is with the positive declination and the second one with the negative declination. Then we use the same algorithm described above on the first group, rotate around the azimuth back to 0° and use the algorithm again on the second group. In Figure 7.7 the trajectory difference from the original method emphasized by red colour is depicted.

In the next section the final measurement sequences are tested in the experiment. Using the same sample and the same light source we will discuss a time consumption

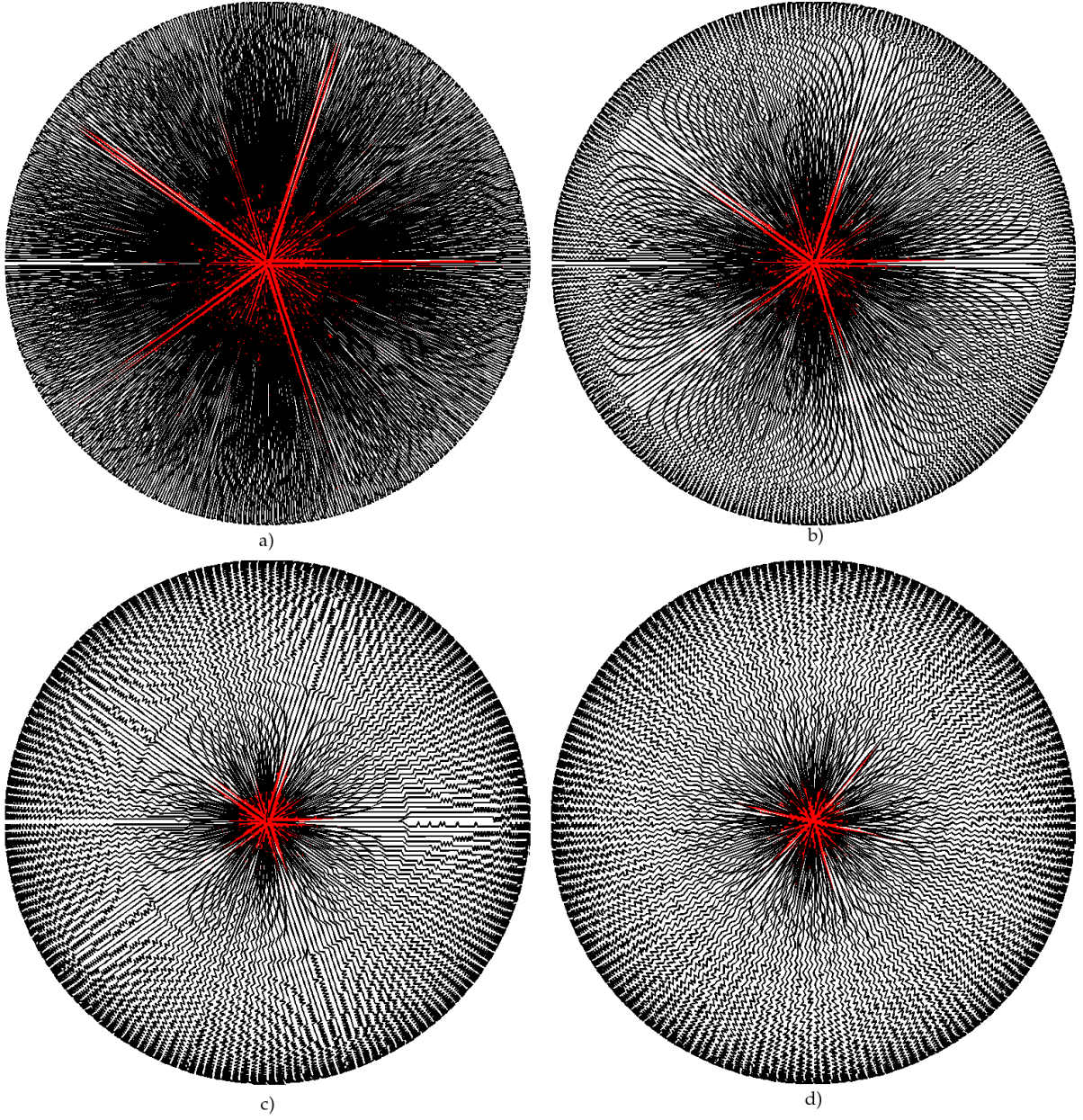


Figure 7.7: Four different measurement sequences. Sequences a), b) and c) are for different widths of azimuth coordinate intervals 0.5° , 1.0° and 2.0° for the respective cases created on the optimized icosahedron breakdown frequency 61 initial system and d) shows the sequence with the azimuth coordinate interval width 2° and the optimized 35296 spiral system initial configuration. The red part is corresponding to the trajectories that are excluded by the improved method.

of the respective measurement, the angular distribution of the scattered light and also the integral value of the scattered energy.

8. EXPERIMENT

In this chapter we will perform measurements with SM II. We will discuss results in terms of improving the total time consumption of measurement and preserving the angular distribution resolution. Further we will introduce the integral power computations and the comparison of results with results obtained with the integrating sphere.

We have received silicon solar cell prefabricates with pyramidal structures as samples. The provider (company Solartec s.r.o.) claims that the angle of pyramids is 120° .

8.1. Time consumption

The first section of this chapter is devoted to the comparison of different approaches to the measurement sequences creation. Table 8.1 shows time needed for execution of the given measurement sequence for the icosahedron points configuration. To classify the sequences we have also calculated the trajectory length which detector performs during the measurement.

Type of the measurement sequence	Time consumed [min]	Trajectory length [m]	Speed [mm/s]
Previously used type of the measurement sequence	244	91.48	6.25
Normal method with the width 0.5°	300	179.82	9.99
Improved method with the width 0.5°	283	157.34	9.27
Normal method with the width 1°	256	94.27	6.14
Improved method with the width 1°	254	86.60	5.68
Normal method with the width 2°	256	68.10	4.43

Table 8.1: Comparison of the different measurement sequences generated for the icosahedron breakdown frequency 61 optimized initial points system and the previously used (old) type of measurement sequence.

There is no improvement in the time consumption. This supports the statement in Chapter 7 where we have considered the previously used measurement method to be very close to the minimal time needed for travelling of the detector over the whole hemisphere. Differences in speeds are caused mostly by the different angular velocities of the respective motor shafts. For the interval width 0.5° the motion is performed primarily by the declination motor. The portion of the motion performed by the azimuth motor raises with the increasing width of the azimuth coordinate interval. Experimental observations and also the experimental data show that the azimuth motor is slower. This results in higher measurement times even for shorter trajectories.

8.2. Angular distribution

We have calculated the sum of absolute differences between the data measured using the previously used measurement sequence and the new ones as a comparison between them. After that we have divided this value by the sum of values measured with the

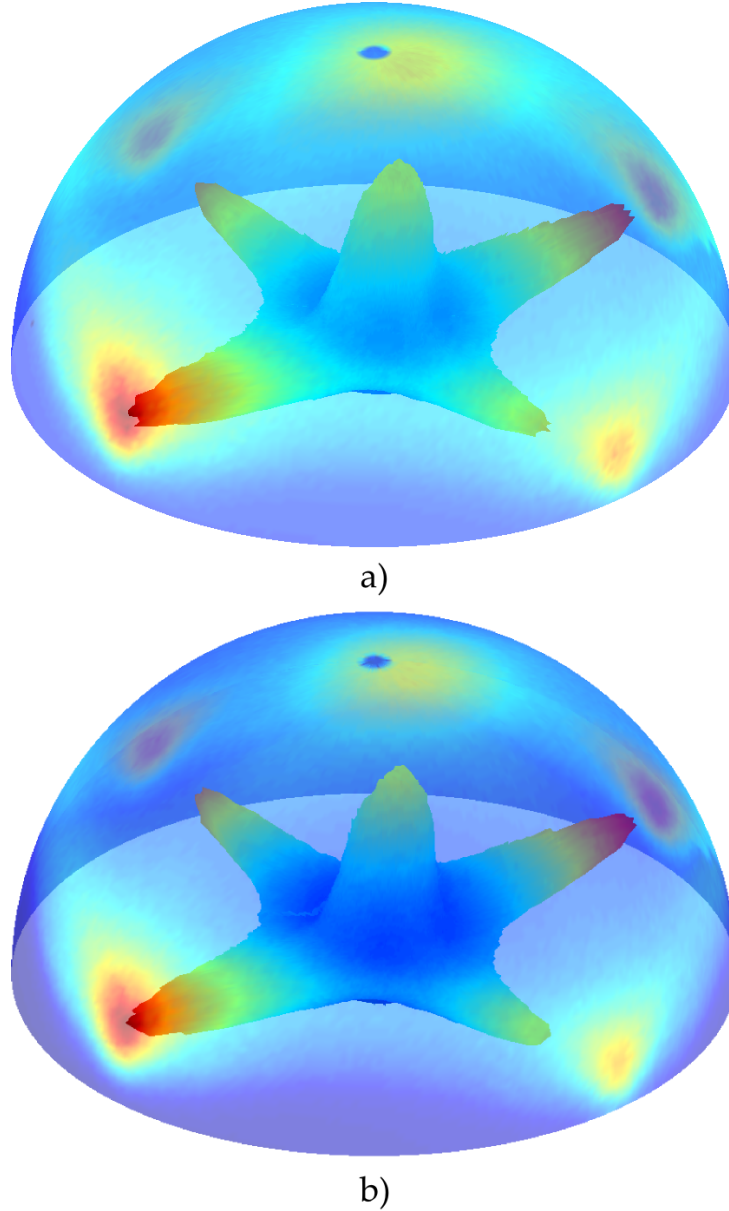


Figure 8.1: Comparison of the angular distribution of the scattered light measured a) using the previously used measurement sequence b) using the icosahedron breakdown system measurement sequence. Both distributions are normalized. The surface of the hemisphere is coloured by the square root of the value measured by the photodiode to emphasize details of the structure of the scattered light.

old method to determine the relative difference. To create a corresponding values from the scattered measurement positions in the case of the new sequences we have used the bilinear interpolation. Table 8.2 shows the values of relative differences for given point configurations. It shows that the optimization does not assure better determination of

the angular distribution. To compare the sequence with the smallest relative difference and the previously used one, we have placed corresponding plots in Figure 8.1.

Type of the sequence	Relative difference [%]
Icosahedron breakdown system	3.41
Optimized icosahedron system	4.41
Spiral points system	5.93
Optimized spiral points system	11.47
Parallel rings system	3.76
Optimized parallel rings system	4.84

Table 8.2: Comparison of the angular distributions measured using the previously used and the new measurement sequences. The relative difference is defined as a ratio of the sum of absolute differences between the data and the sum of data measured by the previously used measurement sequence.

8.3. Comparison with integrating sphere

The last experiment performed was the comparison with the results obtained with the integrating sphere. The photodiode was calibrated using the linear regression equation from [3]. After that we have computed the corresponding area covered by each detector position and we have corrected the respective values measured by the photodiode. Results of the respective measurements are shown in Table 8.3. Results show

Type of measurement	Energy of scattered light [%]
Integrating sphere	17.10
Icosahedron breakdown system	17.01
Optimized icosahedron system	16.22
Spiral points system	18.62
Optimized spiral points system	14.22
Parallel rings system	18.28
Optimized parallel rings system	17.01

Table 8.3: Comparison of the relative amount of energy scattered from the surface measured with SM II and integrating sphere.

that the measurement of the total integrated energy scattered from the surface by means of SM II is valid. Unfortunately the error analysis is not performed and should be studied further. Figure 8.2 shows the corresponding areas calculated for the total integrated energy computation of the icosahedron breakdown system.

8.3. COMPARISON WITH INTEGRATING SPHERE

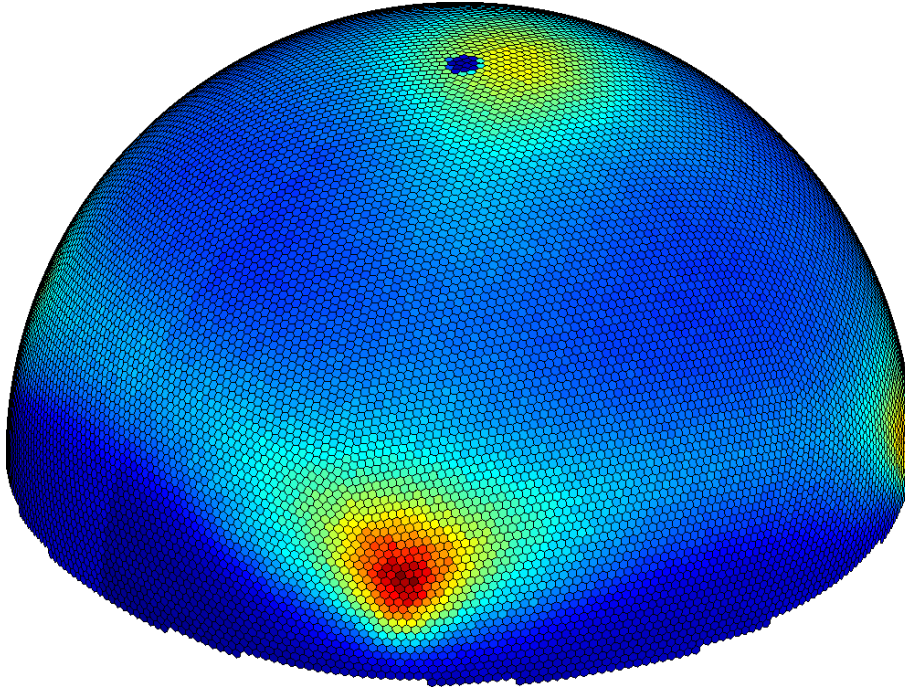


Figure 8.2: Hexagonal tilting as a tool for the correction of the circular detector area. The tilting is generated for the icosahedron breakdown frequency 61 system of initial points.

9. CONCLUSIONS

The aim of this work was to validate and improve the measurement process of the unique device SM II developed in The Laboratory of Coherent Optics, IPE FME BUT. The goal of SM II is to measure the angular distribution of the light intensity scattered from a rough surface of a solid sample. The current measurement process of the angular distribution of the scattered light intensity was well described in Nádaský's Master's Thesis [3]. His work also broached the problem of converting the light intensity into the energy of radiation scattered from a solid surface. He calculated the total energy scattered from a silicon solar cell sample to check the validity of the conversion. But the energy of the incident light was lower than the sum of calibrated values of energy measured in individual detector positions. After that he found out that he has to compensate overlapping of the detector's active areas during the measurement process. Nádaský also suggests in the end of his work that non-overlapping setup of detector positions should be found.

The crucial part of this work concerns with finding the non-overlapping setup of detector positions. A short introduction to the laboratory history and development of SM II is presented in the first chapter. The second chapter deals with describing the SM II and the former type of measurement. Chapter 3 gives mathematical insight into the problem of non-overlapping systems of points on the surface of a (hemi) sphere. The next chapter describes the optimization routine which was developed as one of the approaches for obtaining the non-overlapping setup of detector positions. Chapter 5 shows three approaches of creating initial set of points on a sphere to prearrange better convergence of optimization routine. Features of sets of initial points and the effect of the optimization routine are discussed in Chapter 6. In the following chapter the results from Chapter 6 are used and applied in the real measurement process. The last chapter is devoted to experiments.

Experiments show that the time needed for the measurement is rather prolonged then shortened, like we have expected from the reduction of measurement positions. Nevertheless, one can really shorten the time by speeding up the azimuth motor. The angular distribution comparison shows that most of the measurement sequences results lies within the acceptable range of the relative difference from the previous measurement sequence. The last experiment compares the total energy scattered from the silicon solar cell sample measured by SM II and the integrating sphere. Values are comparable, but the error distribution analysis is missing and should be a subject of future studies.

This work proved that the new approach is valid and comparable with the previous measurement process. Advantages of the new approach are:

- Individual measurement positions are independent (this fact is not assured in the case of the previous measurement process).
- Independence allows us to interpolate or integrate the data. This can be useful in future engineering applications and experiments.
- The resolution is fixed and it is only defined by the ratio of the hemisphere radius and the detector's active area diameter.

- Final results can be used for creating other devices, for example another type of a scattermeter with a static array of detectors.

Results of this work were used in the project "Colour solar cells with high efficiency for architectural applications" (contract number FR-TI1/168). Furthermore the results will be utilized in the future cooperation with the company Solartec s.r.o..

10. BIBLIOGRAPHY

- [1] GRÜNDLING, V. *Návrh a realizace zařízení pro měření rozptylu světla na rovinných povrchích solárních článků*. Brno, 2008. Master's thesis. Brno University of Technology, Faculty of Mechanical Engineering. Supervisor doc. RNDr. Miloslav Ohlídál CSc.
- [2] BRILLA, P. *Realizace zařízení pro měření rozptylu elektromagnetického záření ve struktuře solárních článků*. Brno, 2010. Master's thesis. Brno University of Technology, Faculty of Mechanical Engineering. Supervisor doc. RNDr. Miloslav Ohlídál CSc.
- [3] NÁDASKÝ, P. *Experimentální studium rozptylu světla na povrchích solárních článků*. Brno, 2010. Master's thesis. Brno University of Technology, Faculty of Mechanical Engineering. Supervisor doc. RNDr. Miloslav Ohlídál CSc.
- [4] RAKHMANOV, E.A., E.B SAFF and Y.M. ZHOU. *Electrons on the sphere*. In: ALI, Rosihan M, Stephan RUSCHEWEYH a E SAFF. Computational methods and function theory 1994: 21-25 March 1994, Penang, Malaysia. River Edge, NJ: World Scientific, c1995, pp. 293-309. ISBN 9810221290.
- [5] TAMMES, P. M. L. *On the origin of number and arrangement of the places of exit on the surface of pollen-grains*. Amsterdam, 1930. Doctor thesis. University of Amsterdam.
- [6] HAZEWINKEL, M. *Encyclopaedia of mathematics: an updated and annotated translation of the Soviet "Mathematical encyclopaedia"*. Norwell, MA, U.S.A.: Sold and distributed in the U.S.A. and Canada by Kluwer Academic Publishers, c1988-c1994, 10 ed. ISBN 155608009310.
- [7] BRAUCHART, J. S., D. P. HARDIN and E. B. SAFF. *The support of the limit distribution of optimal Riesz energy points on sets of revolution in $R[\sup 3]$* . Journal of Mathematical Physics. 2007, iss. 48, nr. 12, pp. 122901-. DOI: 10.1063/1.2817823. Available from: <http://link.aip.org/link/JMAPAQ/v48/i12/p122901/s1>
- [8] SAFF, E. B. and A. B. J. KUIJLAARS. *Distributing many points on a sphere*. The Mathematical Intelligencer. 1997, iss. 19, nr. 1, pp. 5-11. DOI: 10.1007/BF03024331. Available from: <http://link.springer.com/10.1007/BF03024331>
- [9] CONWAY, J. H. and N SLOANE. *Sphere packings, lattices, and groups*. 3rd ed. New York: Springer, c1999, lxxiv, 703 p. ISBN 03-879-8585-9.
- [10] CLARE, B. W. and D. L. KEPERT. *The Closest Packing of Equal Circles on a Sphere*. Proceedings of the Royal Society A: Mathematical, Physical and Engineering Sciences. 1986-06-09, iss. 405, nr. 1829, pp. 329-344. DOI: 10.1098/rspa.1986.0056. Available from: <http://rspa.royalsocietypublishing.org/cgi/doi/10.1098/rspa.1986.0056>
- [11] PRESS, W. *Numerical recipes in C the art of scientific computing*. Cambridge: University Press, 1996, 990 p. ISBN 05-214-3108-5.
- [12] KREYSZIG, E. *Advanced engineering mathematics*. 9th ed. Hoboken: John Wiley, c2006, 1094 p. ISBN 04-717-2897-7.

- [13] KUIJLAARS, A. B. J. and E. B. SAFF. *Asymptotics for minimal discrete energy on the sphere*. Transactions of the American Mathematical Society. 1998, iss. 350, nr. 02, pp. 523-539. DOI: 10.1090/S0002-9947-98-02119-9. Available from: <http://www.ams.org/journal-getitem?pii=S0002-9947-98-02119-9>
- [14] HABICHT, W. and B. L. WAERDEN. *Lagerung von Punkten auf der Kugel*. Mathematische Annalen. 1951, iss. 123, nr. 1, pp. 223-234. DOI: 10.1007/BF02054950. Available from: <http://link.springer.com/10.1007/BF02054950>
- [15] CLINTON, J. D. NASA. *Advanced structural geometry studies: Part I - Polyhedral subdivision concepts for structural applications*. 1971, 111 p.
- [16] KENNER, H. *Geodesic math and how to use it*. 2nd pbk. ed. Berkeley: University of California Press, 2003, 172 p. ISBN 05-202-3931-8.
- [17] APPELBAUM, J and Y WEISS. *The packing of circles on a hemisphere*. Measurement Science and Technology. 1999-11-01, iss. 10, nr. 11, pp. 1015-1019. DOI: 10.1088/0957-0233/10/11/307. Available from: <http://stacks.iop.org/0957-0233/10/i=11/a=307?key=crossref.e404e8154c6e8e78c290953c36b37bd4>
- [18] HEISTERKAMP, N., E. ORTJOHANN and J. VOß. *A spatial irradiation measuring system*. In: Thirteenth European Photovoltaic Solar Energy Conference: proceedings of the International Conference, held at Nice, France 23-27 October, 1995. Bedford: H.S. Stephens, 1995, pp. 1926-1929. ISBN 0-9521452-6-X.

11. LIST OF SYMBOLS AND ABBREVIATIONS

α	detector elevation angle
C	number of rings
ε	value of potential at equilibrium of Lennard-Jones potential
η	detector viewing angle
E	number of edges
E_s	Riezs s -energy
F	number of faces
\mathbf{F}_{net}	net force
\mathbf{F}_n	normal component of the net force
\mathbf{F}_t	tangential component of the net force
γ	detector azimuth angle
h	step of differentiation
h_k	z -coordinate of a k -th spiral point
k	spring constant
λ	wavelength of the inciednt radiation
MPI	Message Passing Interface protocol
ν	breakdown frequency
N	number of points
n	total number of calculations
SM I	first generation of Scattermeter
SM II	second generation of Scattermeter
Φ	scalar potential of a set of points
ϕ	azimuth angle
φ	scalar potential
Q	arbitrary constant
Q_1	arbitrary constant
R	radius of the sphere

r	mutual distance of positions
r_m	equilibrium distance of Lennard-Jones potential
\mathbf{r}	position vector
s	Riezs s -energy factor
θ	declination angle
V	number of vertices
w	number of workers
w_i	number of tasks assigned to i -th worker
X_N	set of points
ζ	cross-sectional arc angle